General Disclaimer

One or more of the Following Statements may affect this Document

Quarterly Report

EBIC INVESTIGATION OF HYDROGENATION OF CRYSTAL DEFECTS IN EFG SOLAR SILICON RIBBONS.

Quarterly Report

Period: Jan 1, 1983 to March 31, 1983

JPL Contract No. 956046, Report #5

Prepared by:

T. Sullivan and D.G.Ast

Department of Materials Science and Engineering
Cornell University
Ithaca, NY 14853.

May 1983

ABSTRACT

Changes in the contrast and resolution of defect structures in 205 Ohm-cm EFG polysilicon ribbon subjected to annealing and hydrogenation treatments were observed in a JEOL 733 Superprobe scanning electron microscope, using electron beam induced current (EBIC) collected at an Al Schottky barrier. The Schottky barrier was formed by evaporation of Al onto the cleaned and polished surface of the ribbon material. Measurement of beam energy, beam current, and the current induced in the Schottky diode enabled observations to be quantified. Exposure to hydrogen plasma increased charge collection efficiency. However, no simple causal relationship between the hydrogenation and charge collection efficiency could be inferred, because the collection efficiency also displayed an unexpected thermal dependence. Good quality intermediate-magnification (1000X-5400X) EBIC micrographs of several specific defect structures were obtained. Comparison of grown-in and stress-induced dislocations after annealing in vacuum at $500^{\circ}C$ revealed that stress-induced dislocations are hydrogenated to a much greater degree than grown-in dislocations. The theoretical approximations used to predict EBIC contrast and resolution may not be entirely adequate to describe them under high beam energy and low beam current conditions.

CONTENTS

LIST OF TABLES

LIST OF FIGURES

I. INTRODUCTION

The scanning electron microscope (SEM) is a highly versatile instrument which is widely used both in research and industrial applications. In the SEM an electron beam focused to a spot from 70Å to 1 µm in diameter scans horizontally across the specimen (see Fig.1.1). Signals generated by the interaction of the beam with the specimen (e.g. backscattered electrons) are used to modulate the brightness of a cathode ray tube (CRT) display screen scanned synchronously with the SEM beam.
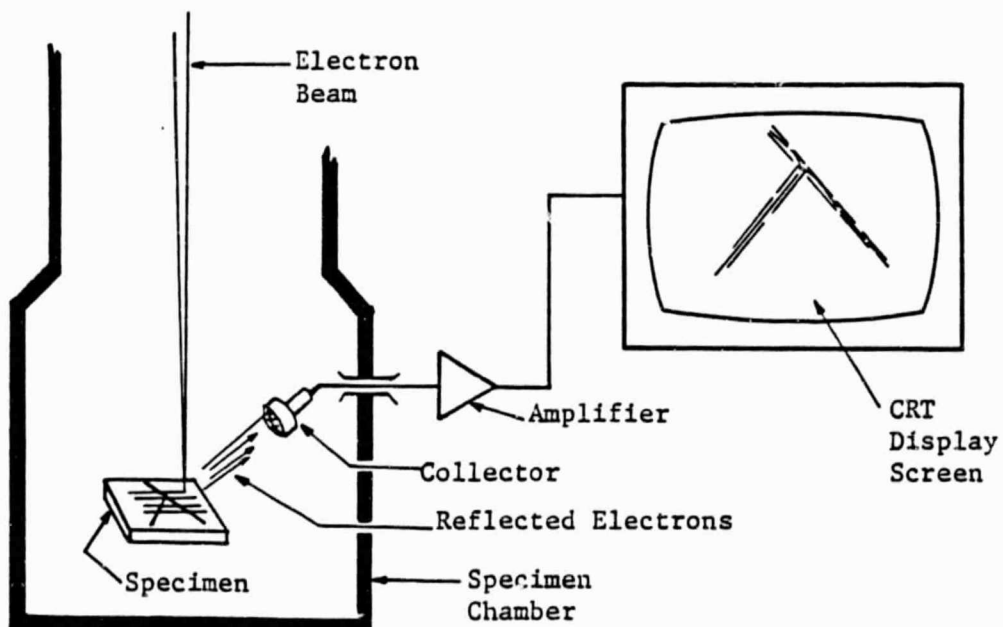
Fig. 1.1. Schematic representation of formation of an SEM image.

Processes that occur during irradiation of the specimen surface include backscattering, secondary emmission, ionization, and phonon generation. Most of the incident (primary) electrons penetrate into the

1

specimen losing energy through electronic collisions, while the remainder are reflected at the surface (backscattered electrons). The intensity of the electrons backscattered into a given solid angle depends on the specimen surface topography. A signal formed from the collection of backscattered electrons can therefore be used for imaging surface features. Penetrating electrons lose energy through inelastic collisions with bound electrons. These collisions fall into two classes according to the amount of energy lost by the primary electron: 1) ionizing collisions which eject bound electrons from their orbits; 2) non-ionizing collisions which generate phonons and heat up the specimen. Following ejection of inner shell electrons, transitions of the outer shell electrons into the vacant inner orbitals are often accompanied by the emmission of an electron (instead of a photon), called an Auger or secondary electron. Electrons with energies below 50 eV can escape from several tens of Angstroms below the specimen surface. They contain information about the near-surface region and are used to form secondary electron images. The primaries that are not reflected and the secondaries that do not escape form electron-hole pairs in the specimen which can be used to probe the spatial variation of minority carrier lifetime.

The SEM is widely used as a tool for characterizing the electrical behavior of semiconductor materials and devices. A common industrial use employs the voltage contrast technique to examine large scale integrated circuits for causes of malfunction [1]. When such a circuit is active, the voltages of surfaces with the same material composition vary from position to position depending on the state of the corresponding circuit element. Secondary electrons emitted from neighboring regions of like composition but different voltages will exhibit corresponding differences in their

energies and will produce fluctuations in the output of the secondary electron detector as the beam transits the specimen. Modulation of the display screen brightness by this output produces the voltage contrast.

The experimental work to be presented is based on another technique, electron-beam-induced current (EBIC), which is commonly used to measure semiconductor material properties and to study defect structures. The incident electron beam is used here to create excess concentrations of hole-electron pairs in the vicinity of a diode formed by a p-n junction or a Schottky barrier. Excess carriers that are created in or diffuse into the depletion layer of the diode are collected by the built-in field, generating a current in an external circuit. Modulation of the display screen brightness by this signal forms a picture of the charge collection efficiency over the specimen surface. Enhanced recombination occuring at crystalline imperfections reduces both the collected current and the current in the external circuit creating dark areas in the image.

Charge collection with a Schottky barrier diode, first used by T. Cass in 1973 [2], is achieved by the vacuum deposition of a thin layer (300Å) of metal such as aluminum (Al), onto a polished semiconductor surface. The metal-semiconductor interface produces a depletion layer in the semiconductor immediately adjacent to the metal. The electron beam penetrates through the metal film into the semiconductor to generate excess carrier pairs which are then collected by the built-in field of the depletion layer. The advantages of this method are 1) that no heat treatment is required which leaves heat sensitive defects unaltered, and 2) that near-surface defects can be imaged with better resolution and contrast than when the diode is located deeper in the material (as with a p-n junction). The resolution improves because the volume over which electrons

scatter is smaller at lower energies and lower beam energies suffice to image near-surface defects. The proximity of the excess pairs to the depletion layer at these lower energies also increases the carrier collection efficiency and produces higher contrast levels.

The specimens used in our experimental work were sections of polycrystalline silicon (polysilicon) ribbon, grown for use in solar cell research. Nearly ideal solar cells can be fabricated on single crystal silicon wafers, but this material is too expensive to use for mass production. Growing the silicon (Si) in ribbon form (long flat strips) eliminates the time and material loss incurred in slicing wafers, and decreases cell cost. The serious disadvantage to the ribbon is its polycrystallinity and high density of crystal defects. The wafers contain grain boundaries, dislocations, twins, stacking faults, and SiC inclusions. Many of these defect structures are known to be sites for enhanced excess carrier recombination, and the presence of such defects will lower the charge collection efficiency. EBIC microscopy of polysilicon ribbon with a Schottky barrier can identify the types and concentrations of the various electrically active defects. Classification of defect types may reveal patterns that would suggest methods of avoiding their formation or neutralizing their negative effects.

One such method currently being studied is exposure of Si to H. Both molecular (H_2) and ionized hydrogen have been found to reduce the electrical activity of several types of defect. Hydrogen treatment has been applied under a variety of conditions to a number of different materials. Variations in plasma pressures and methods of excitation, doping levels, types and concentrations of defects, thermal history of the Si, length of exposure to H, and specimen preparation processes all seem to

influence the results. Nonetheless there is consensus that hydrogenation under suitable circumstances improves charge collection efficiency.

One goal of our work was to document changes in the electrical activity in edge-defined-film-fed grown (EFG) polysilicon ribbon under plasma annealing. We also wanted to discover if hydrogenation would be useful in aiding the characterization of defects.

Before describing the experiment and discussing the results, a more detailed discussion of the principles of EBIC will be presented, followed by a brief review of the work in hydrogenation.

II. PRINCIPLES OF EBIC MICROSCOPY

II.A. GENERAL BACKGROUND

Conceptually, the production of an EBIC signal is elementary. A beam of intermediate energy electrons (5 KeV $< E_b < 50$ KeV) is focused on a semiconductor surface containing a diode formed by a p-n junction or a Schottky barrier (Fig.2.1). Most of the incident electrons penetrate into the semiconductor losing their energy through collisions with bound electrons and lattice nuclei. The maximum range R of the electrons depends both on the beam energy E_b and the average atomic weight of the material. Colliding electrons scatter over a wide range of angles producing excess carriers throughout a small volume of the crystal. This volume -- called the generation volume -- is centered about the beam axis and in the first approximation is spherical, so that its diameter is also R. The excess carriers are hole-electron pairs formed by the ionization of lattice atoms. An electron (hole) that has been freed from its bound state is often said to have been excited from the valence (conduction) band into the conduction (valence) band. When these excess pairs are generated in a region of the crystal containing no electric fields, they recombine at a rate which is inversely proportional to the minority carrier lifetime. When the generation volume is partially contained within the depletion layer, as in Fig.2.1, two effects occur. First, the excess carriers within the depletion layer are swept apart by the built-in field and captured, preventing recombination. Second, a fraction of the minority carriers created outside of the depletion layer, will diffuse towards the junction and will be collected by the built-in field. When the diode is

6
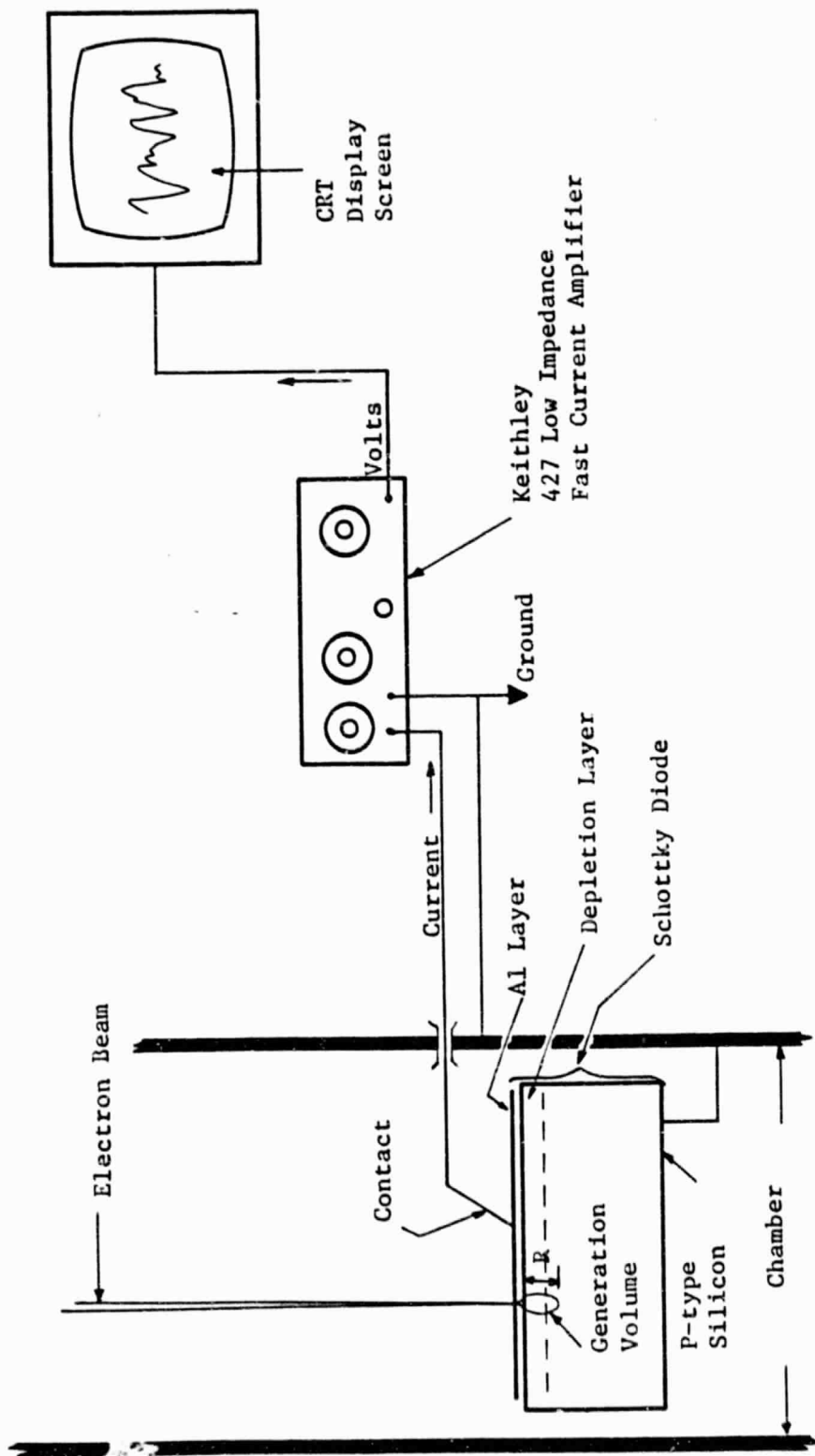
Fig. 2.1. Production of an EBIC image using a Schottky barrier diode.

short-circuited, a current flows in the external curcuit, is converted into a voltage signal by a low-impedance current amplifier and used to modulate the z-axis signal (brightness) of the microscope CRT display screen. The horizontal and vertical sweep rates of the CRT display are synchronized with those sweeping the beam across the specimen in the microscope.

Inhomogenieties within the semiconductor such as inclusions, dislocations, etc., are associated with locations or sites known as recombination centers. These sites become sinks for the injected carriers, locally decreasing the minority carrier lifetime and diffusion length relative to those in the perfect crystal. When the generation volume encounters such regions of enhanced recombination, the current into the recombination centers is lost from that generated in the external circuit, resulting in a reduction of intensity displayed on the CRT. Thus the display screen image is a spatial map of the collection efficiency of injected carriers in the near-surface (0-10 μm) region of the specimen. The resolution of this technique is roughly equal to the generation volume diameter R and ranges from 0.1-10 μm. This subject will be treated in more detail below. The resolution is completely inadequate to resolve actual lattice defects such as dislocations, whose dimensions are on the order of Angstroms. EBIC images therefore represent the electrical influences of a given defect and not its atomic structure. For this reason, positive identification of particular defects cannot be established by the analysis of EBIC micrographs alone. But correlation of EBIC results with observations from transmission electron microscopy (TEM) -- high-voltage electron microscopy (HVEM) for thick specimens -- provides a powerful tool to identify the specific defects that produce particular types of electrical contrast [3,4].

II.B. EXCESS CARRIER GENERATION

In order to derive quantitative results from EBIC signals one needs to know the quantity of hole-electron pairs generated by the incident beam. Since some of the beam contributes to processes other than carrier pair creation, and since some carriers are lost through Auger emission, a quantitative understanding of each of these factors is required.

II.B.1. SPECIMEN CURRENTS AND ELECTRON LOSS MECHANISMS

Aside from the EBIC current, three currents flow out of the specimen: (1) the so-called specimen current, I_s, which flows to ground through the specimen holder, (2) backscattered electrons, and (3) emitted secondary electrons. Backscattered electrons are primary electrons which are scattered both elastically and inelastically from the crystal. Secondary electrons are produced in two steps. First a primary electron collides with an inner shell electron of a lattice atom, imparting to it sufficient energy to elevate it from the valence band to the conduction band. Transition of an outer shell electron to the empty orbital in the inner shell (corresponding to a transition from a shallow valence band level to a deep one) is more likely to be accompanied in light elements by the emission of an electron rather than an X-ray. This electron is the secondary (or Auger) electron.

Backscattered electrons can have energies as low as a few eV if they undergo many collisions before being deflected back out of the crystal. On the other hand, secondary electrons with KeV energies can be emitted. Since no way exists to distinguish highly energetic secondaries from

elastically scattered primaries, or weakly reflected primaries from low energy secondaries, backscattered electrons are designated by convention [5] as those having energies greater than 50 eV, while those with energies less than 50 eV are designated as secondaries. This division is not entirely arbitrary since most backscattered electrons have energies near the beam energy, whereas most emitted secondaries have energies below 30 eV, as will be discussed below.

Primary electrons which enter the speimen produce an excess charge in the specimen. (This is to be distinguished from the generation of excess carriers which are created in hole-electron pairs which leave the crystal electrically neutral.) The specimen is usually grounded to prevent the accumulation of this excess charge, and the current to ground is just I_s, the specimen current mentioned above. If no backscattering or secondary emission occurred, I_s would equal the beam current I_b. Backscattering reduces I_s by reducing the portion of the beam that actually enters the crystal, while emitted secondaries reduce I_s by providing an alternate path to ground. I_s is a readily measured parameter which is sometimes used to calculate the magnitude of the excess charge generated by the beam. A clear understanding of the ways that backscattering and secondary emission influence I_s is essential in order to properly interpret calculated results.

II.B.1.a. BACKSCATTERING

For a given material and beam energy, and for normal beam incidence, some fraction of the incident beam will be reflected. Not all of the reflected electrons undergo purely elastic collisions. Most will be

involved in several collisions in the near-surface region before they are deflected back out of the crystal, with energies which will range from 0 eV to E_b. To find the number of excess carriers generated by the beam, the fraction of the beam energy imparted to the crystal must be known. Thus we need to know both the fraction of reflected electrons as well as their average energy loss. Measurements made by Bishop [6] show that the fraction of backscattered electrons η for aluminum ($Z = 13$) varies little with beam energy:

E_b	η
10 KeV	.171
30 KeV	.155

Sternglass [5] shows even less variation for the range 2 KeV $< E_b <$ 5 KeV. Bishop also shows that the relative mean energy loss of backscattered electrons is essentially independent of beam energy for a given material. For Al this is approximately $0.42E_b$. Thus the mean energy of the reflected primaries is $(1-.42)E_b = .58E_b$, and therefore the net energy loss from the beam due to backscattering is $(0.58) \eta E_b = 0.1E_b$. Since our Schottky barrier diodes were made with thin Al layers, these numbers are approximately correct if scattering from the underlying Si is neglected.

II.B.1.b. SECONDARY EMISSION

As mentioned above, secondary electron emission is generated by ionization of the K or L shell of a lattice atom, the K level being generally more probable. The secondary electron is emitted simultaneously with the transition of an L electron into the empty K shell orbital leaving the atom doubly ionized in the L shell. The emitted electron then has the

energy of the K shell minus the ionization energy of the L-III, L-III state
[7]. For Al, the K level energy is 1562 eV and that of L-III is 7.27 eV
[8], so the Auger electron will have an initial energy in excess of 1500
eV. Each secondary electron and the corresponding ionized atom form a
carrier pair. These secondary electrons may be emitted isotropically
at where in the generation volume where colliding electrons have sufficient
energy to ionize the K shell, and proceed to collide with other electrons
to generate still more electron-hole pairs. At this point secondary
electron kinetic energies in the KeV range might seem to contradict the
convention that designates emitted secondaries as those with energies 50 eV
or less. The key to this paradox lies in the dependence on energy of the
mean free path of the electron within the crystal.
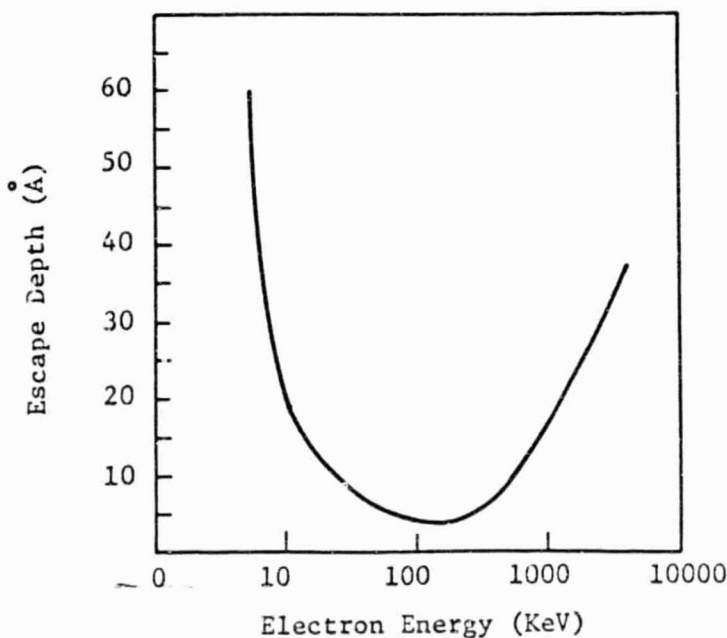
Fig. 2.2.

Electron escape depth
as a function of energy
(Ref. [9]).

Fig.2.2 is a schematic representation of the escape depth of electrons as a
function of their energy [9]. The escape depth for energies between about

40 eV and 200 eV is small, about 5Å. For energies < 40 eV the escape depth increases rapidly to about 60Å near 5 eV. For energies > 200 eV the escape depth increases slowly with energy, so that at 1000 eV it is still less than 20Å. Since electron penetration depths at E_b = 1 KeV are generally 100-200Å, most of the highly energetic secondaries are not able to reach the specimen surface. The electrons most likely to be emitted are in the first few layers of atoms and have energies below 50 eV. According to Sternglass [5], more than 95% of all emitted secondaries have energies < 30 eV.

At low beam energies a very large percentage of secondaries are emitted from the specimen, and the emitted current may exceed the incident current. Under these conditions, charge would have to flow from ground into the specimen to maintain charge neutrality, and I_s would reverse polarity. (The crossover is used extensively in voltage contrast of operating integrated circuits since no charge is injected into the circuits.) This situation is unlikely to occur at energies used in EBIC, but the extreme serves to illustrate that measurement of the specimen current alone is not sufficient to calculate the rate of excess carrier creation.

Czaja [10] measured the beam current I_b and the specimen current I_s and calculated

$$(2-1) \quad \delta = \eta + \Delta = (I_b - I_s)/I_b$$

which is the loss of electrons from the specimen due to backscattering (η) and secondary emission (Δ) expressed as a fraction of the beam current. Fig.2.3 shows δ as a function of beam energy for Al and Si [10]. Note that

η is constant over the energy range and is given as $\eta = 0.15$ for Al, in general agreement with Bishop [6]. Czaja's curve for δ is given to a good approximation by

$$(2\text{-}2) \qquad \delta = \underset{(\Delta)}{(163 \text{ KeV})/E_b} + \underset{(\eta)}{15}$$

for 5 KeV $< E_b < 40$ KeV. Hence for $E_b = 5$ KeV, $\delta = 47.6\%$. Hence about half of the beam current flows to ground through the specimen and the other half reaches ground through backscattering and secondary emission.
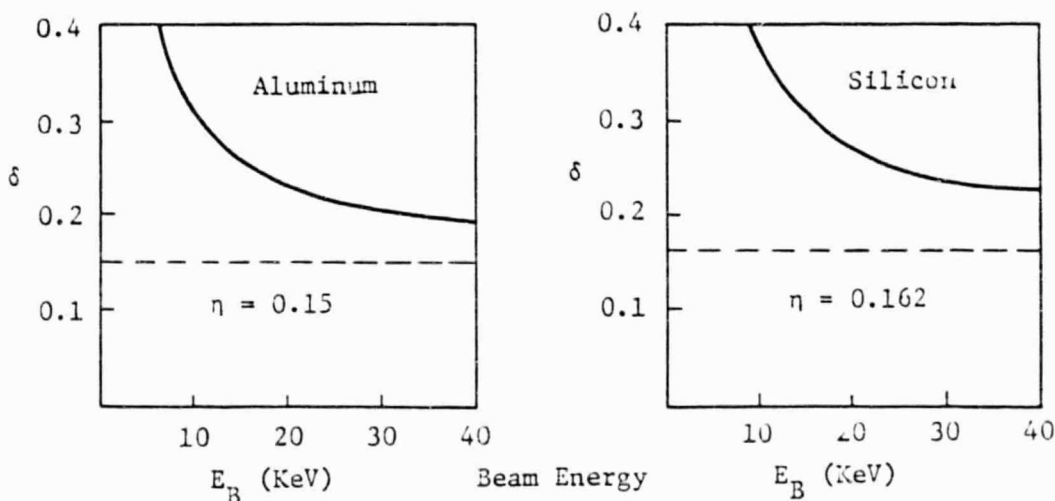
Fig. 2.3. Total electron emission from the surface of a speci-
men irradiated by an electron beam, for Al and Si,
expressed as a fraction of the beam current =
$\delta = (I_b - I_s)/I_b$. η = backscattered fraction.

II.B.2. ENERGY OF CREATION PER HOLE-ELECTRON PAIR

The minimum energy needed to form a single hole-electron pair is just that of the forbidden gap E_g which is 1.12 eV in Si. But other factors

must be considered when determining how many pairs can be generated by a single primary electron. A model proposed by Shockley [11], considers two kinds of collisions along the path of the primary electron: ionization collisions in which the electron loses E_i, the energy necessary to ionize an outer electron; and phonon producing collisions in which kinetic energy is converted into phonon energy (heat). Several phonon producing collisions are thought to occur between ionizing collisions. Denoting the average number of phonons generated between ionizing collisions by r, and the energy of a (Raman) phonon by E_p, the average energy dissipated in phonon producing collisions per ionization is rE_p. Experimentally, E_p = 0.063 eV (for Si) and r = 17.5 phonons/ionization, so rE_p = 1.1 eV. Finally, a residual energy $E_f < E_i$ is left after the last pair-producing collision. When E_f is averaged over all energies between 0 eV and E_i in the first Brillouin zone, $E_f = 0.6E_i$. Adding all of these contributions

$$
\begin{aligned}
\text{(2-3)} \qquad E \text{ (pair)} &= E_i + rE_p + 2E_f \\
&= E_i + 2(.6)E_i + rE_p \\
&= 2.2E_i + rE_p \\
&= 3.52 \text{ eV}
\end{aligned}
$$

Experimental measurements [12] set E (pair) at about 3.62 eV for Si at room temperature, in agreement with this model. Later authors use a somewhat higher value of 3.67 eV [2]. Hence the number of pairs generated per 5 KeV primary electron in Si would be about 5 KeV/3.62 eV = 1381 pairs.

Assuming that all generated pairs are collected by the Schottky diode, the collected current would be given by

$$
\begin{aligned}
\text{(2-4)} \qquad I_{cc} &= 1381(1-0.58 \ n)I_b - \Delta I_b \\
&= [1381(0.9) - 33]I_b \\
&= 1210 I_b
\end{aligned}
$$

where the factor $(1-0.58\,\eta)$ accounts for the loss of pair generation due to backscattered electrons and Δ accounts for the loss of pairs due to the emitted secondaries. This last factor is somewhat uncertain because no attempt has been made to assess the average energy of the emitted secondaries -- it was taken to be on the order of 3 - 4 eV. However, the analysis illustrates that the correction to I_{cc} for secondary electron emmision is only a few percent. Finally, it is interesting to note that the diode acts as a current amplifier with a gain of about 1000.

II.C. ELECTRON RANGE AND ENERGY DISSIPATION

Calculations of the electron penetration depth (range) and energy dissipation within the target material [13] do not always agree since they employ different definitions and hypotheses. However the treatment by Everhart and Hoff [14] is commonly referenced and is suitable as an introduction because it pertains to the elements $(10 < Z < 15)$ and beam energies $(5 < E_b < 25$ KeV) with which we are concerned. The calculations are supported by excellent experimental results and neglect the effects of secondary electron emission. Everhart and Hoff define the range R after Gruen [15] as the intersection of the tangential extension to the right leg of the depth-dose curve (Fig.2.4), rather than the maximum penetration depth.

For an Al - SiO$_2$ - Si system

(2-5) $R = 0.0171 E_b^{1.75}$ μm   (E_b in KeV)

was found to be accurate for beam energies 5 KeV $< E_b <$ 25 KeV. By

measurement of the current through a layer of SiO_2 of known thickness generated by a beam held at constant current and energy, the number of carriers being generated was inferred.
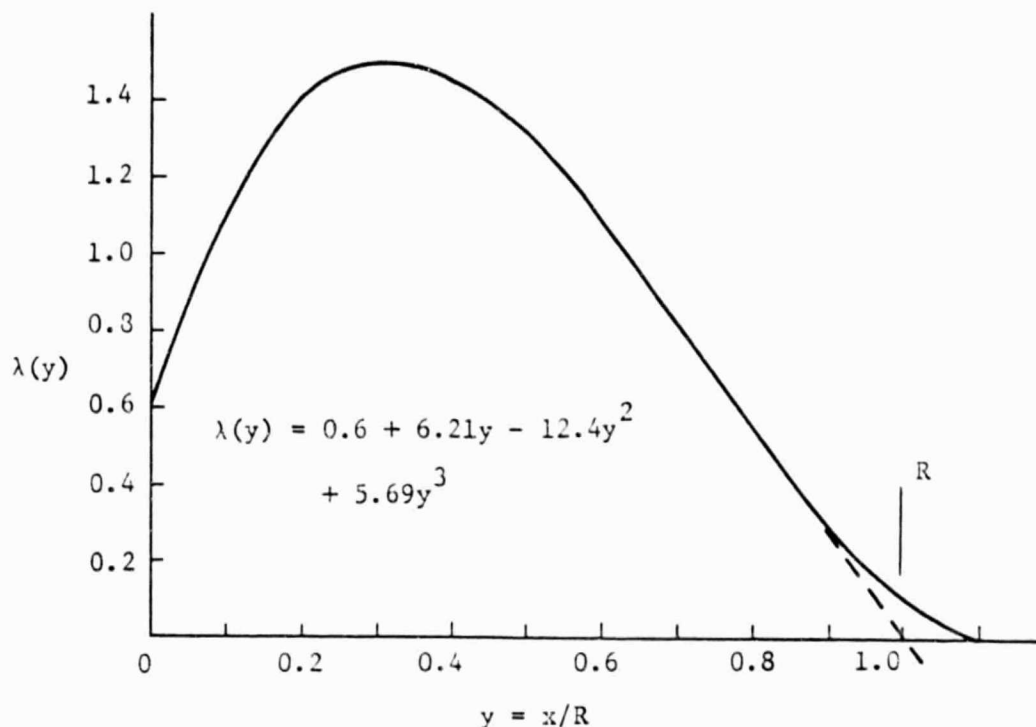
Fig. 2.4. Normalized depth-dose distribution showing the range R of the most energetic electrons [14].

Repeating this procedure at several energies, Everhart and Hoff developed a polynomial expressing the energy dissipated by the beam as a function of depth. The polynomial is expressed as

$$
\begin{aligned}
(2\text{-}6) \qquad \lambda(y) &= d(E/fE_b)/d(x/R) \\
&= (R/fE_b)/(dE/dx) \\
&= 0.6 + 6.21y - 12.4y^2 + 5.69y^3
\end{aligned}
$$

where E/fE_b is the normalization with respect to the fraction of the beam energy fE_b actually transmitted to the crystal, and x/R is the normalization with respect to the electron range. The value of f used by

Everhart and Hoff [14] is 0.9 and was obtained by subtracting off the $0.1E_b$ of the beam energy lost due to backscattering, following Bishop's work discussed above (f = 0.58 η = (0.58)(0.17) = 0.1). $\lambda(y)$ is graphed in Fig.2.4 showing R as the intersection with the y-axis of the tangent to the straight region of the right leg of the curve as mentioned above.

The number of hole-electron pairs generated per primary electron in a layer of material with thickness dx is given by

(2-7) $N(x) = (1/3.62 \text{ eV})(dE/dx) = (fE_b/eR) \lambda(y)$.

$N(x)$ is shown in Fig.2.5 for beam energies of 5,7,10,15,20, and 30 KeV. Good empirical agreement with calculations was obtained in the energy range 8-20 KeV justifying the neglect of emitted secondaries, since large deviations would have appeared between calculated and experimental values in precisely this range.

A study of the radial energy dissipation of the beam was made [16-18] by exposing poly-(methyl methacrylate), PMMA, to an electron beam for several different durations. At critical exposure levels X_c (KeV/cc), the fraction of broken bonds in the polymer chains becomes sufficiently large to permit dissolution in a suitable solvent. Material exposed to doses in excess of X_c dissolves, leaving behind material exposed below X_c. Most of the energy dissipation was found to occur in a narrow cylindrical region about the beam axis. As the electrons gradually lose energy, wider angle collisions occur and the excitation volume begins to broaden. At lower energies this broadening becomes gradually spherical (Fig.2.6a) while at higher energies the shape adopts a more teardrop form (Fig.2.6b). This is expected, since the position of peak energy dissipation shifts to deeper levels as beam energy increases, as shown in Fig.2.5. Fig.2.6 shows

Fig. 2.5.

Number of hole-electron pairs generated per primary electron as a function of electron penetration range for six different beam voltages. Also shown is the envelope of peak pair production as a function of energy $(N(x)_{max} = 21.87 \times 10^3 E_B^{-.75})$.

$R_{5 \text{ KeV}} = 0.286$ µm

$R_7 = 0.515$

$R_{10} = 0.962$

$R_{15} = 1.96$

$R_{20} = 3.23$

$R_{30} = 6.58$

Envelope

Electron Penetration Range. $R = 0.0171 E_B^{1.75}$ (µm)

Hole-electron Pairs per Primary Electron per µm $N(x) \times 10^3$
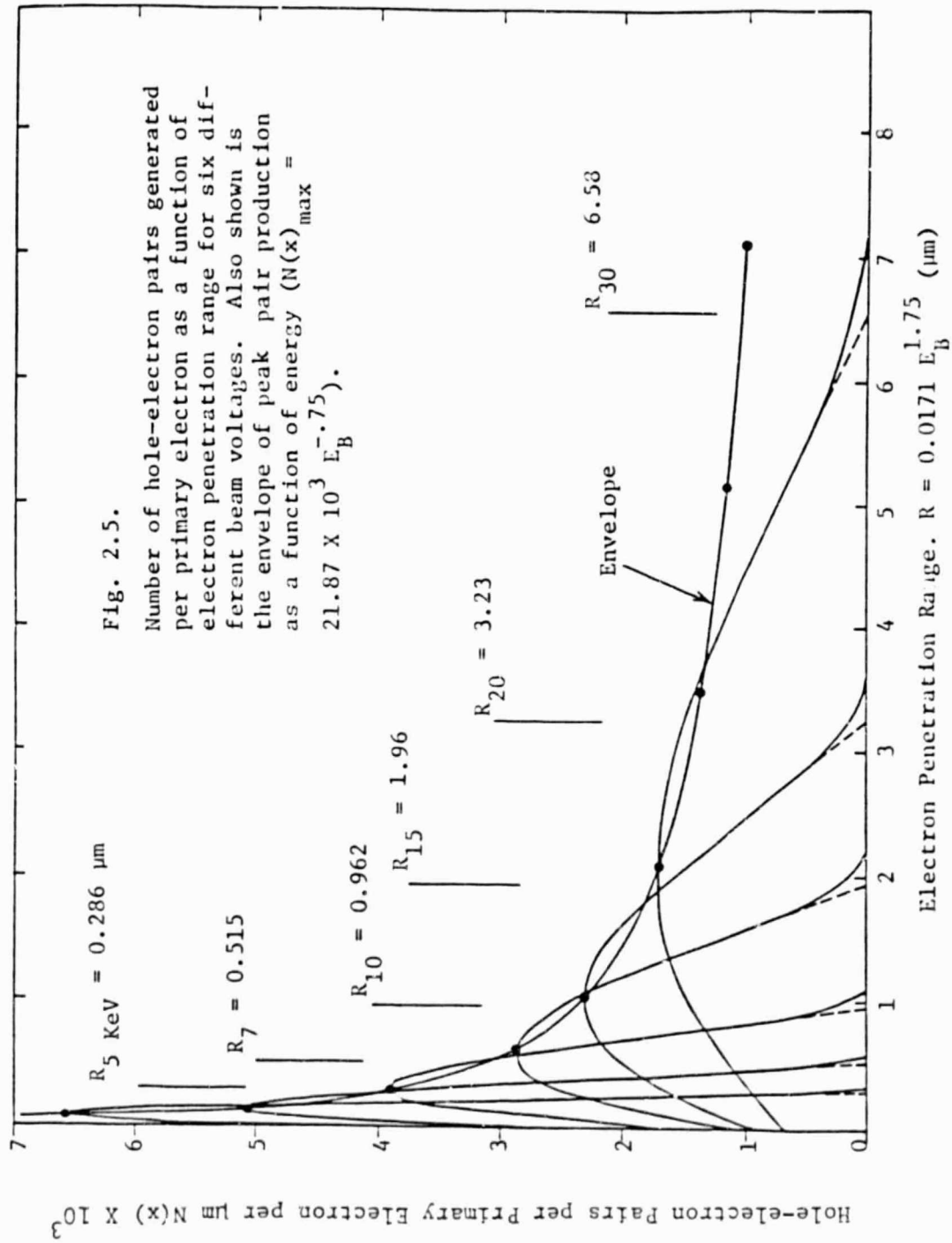
equi-energy contours of generation volumes in PMMA for 14.86 KeV and 29.5 KeV respectively [17]. The initial energy loss occurs mostly by electronic interactions in which the primary electron excites valence electrons into the conduction band with little momentum transfer. Subsequent energy loss is mostly due to collisions which involve more substantial momentum transfer and scattering, causing the generation volume to broaden.

(a)
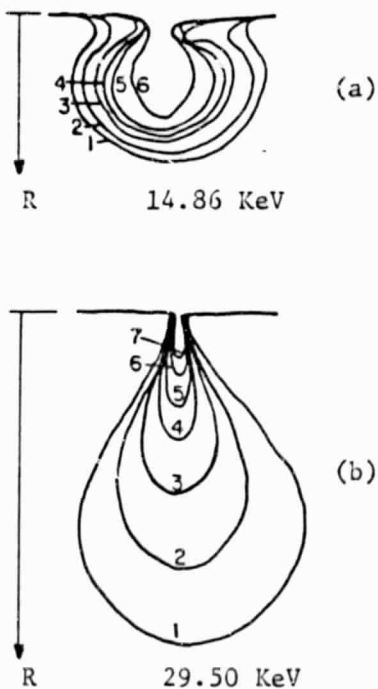
R   14.86 KeV

Fig. 2.6.

Energy dissipation profiles in PMMA for beam energies of a) 14.86 KeV and b) 29.5 KeV. Different contours were obtained through variation of exposure time to the beam [17].

(b)

R   29.50 KeV

One noteworthy characteristic of the energy dissipation function is that the peak dissipation decreases exponentially with increasing energy, even though the total energy dissipation grows linearly with beam energy (see Fig.2.5 showing the envelope for peak pair production). With I_b constant, a greater pair production density can therefore be achieved at lower energies.

II.D. DEFECT IMAGING

II.D.1. GENERAL CONSIDERATIONS

The collection efficiency, e_c, i.e. the ratio of the number of carriers collected to the number generated, depends on the recombination rate near the generation volume, and the size of the generation volume relative to the depletion layer width x_d. Two limiting conditions are of interest: $R < x_d$, where the generation volume is completely contained within the depletion layer; and $R > x_d$, where the generation volume extends beyond the depletion layer. For $R < x_d$, low carrier concentrations, the absence of all but point defects in the depletion layer, nearly all of the generated charges are collected and $e_c = 1$. As an example, consider 200 Ohm-cm Si. The depletion layer width is about 2.68 μm [19] and the average electric field is therefore [20]

$$(2-8) \quad E_{ave} = E_{max}/2 = (qNx_d)/(2K_s e_o)$$
$$= \frac{0.5(1.6 \times 10^{-19} \text{ C/e-})(10^{14} \text{ e}^-/\text{cc})(2.68 \times 10^{-04} \text{ cm})}{(11.7)(8.89 \times 10^{-14} \text{ coul/V-cm})}$$
$$= 2.086 \text{ KV/cm}$$

which means the drift velocity v_d in the depletion layer is

$$(2-9) \quad v_d = 3 \times 10^6 \text{ cm/sec} \quad \text{for electrons and}$$
$$\quad\quad = 1 \times 10^6 \text{ cm/sec} \quad \text{for holes [21].}$$

Thus the carrier is swept out of the depletion layer in less than $x_d/v_d = 10^{-10}$ seconds. For materials with bulk lifetimes of 10 to 100 nsec (typical for Si), recombination within the depletion layer will be negligible. However, this is no longer true for high concentrations of excess carriers and for a high density of point defects.

Using equations from Shockley and Read [22], Miller and Gibson [23]

calculated the decrease in relative lifetime (with respect to bulk lifetime τ_0 for low carrier densities) as a function of carrier density for recombination centers at two different energy levels below the conduction band (Fig.2.7).
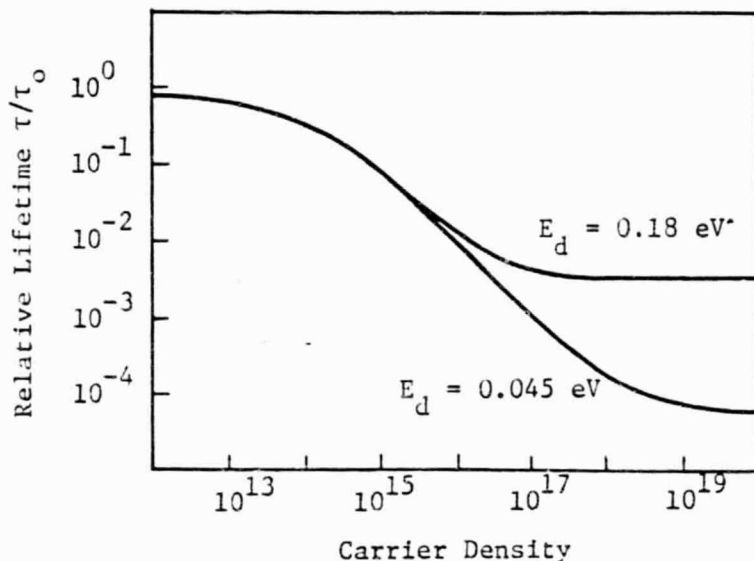
Fig. 2.7.

Relative carrier lifetime as a function of excess carrier density for two different defect levels [25].

The relationship is given by

$$(2\text{-}10) \qquad \tau/\tau_o = \frac{[1 + n_t(\tau_{po} + \tau_{no})/\{\tau_{po}(n_o+n_1) + \tau_{no}(p_o+p_1)\}]}{[1 + n_t/(n_o+p_o)]}$$

where τ_{po} and τ_{no} are the lifetimes of holes in a highly n-type material and electrons in a highly p-type material at the recombination centers under study, n_o and p_o are the equilibrium concentrations of electrons and holes of the specific material, and n_1 and p_1 are the equilibrium concentrations of carriers that would exist if the Fermi level E_F were equal to the trap level E_T. Assuming $\tau_{po} = \tau_{no}$, and considering an n-type material with $E_i < E_T < E_c$ (E_c = energy of the conduction band edge, $E_i = 0.5E_g$, the gap energy), eqn. (2-10) becomes

$$(2\text{-}11) \quad \tau/\tau_o = \frac{1 + 2n_t/(n_o+n_1)}{1 + n_t/n_o}$$

$$= \frac{1 + a\, n_t}{1 + c\, n_t}.$$

In the limit of large n_t

$$(2\text{-}12) \quad \tau/\tau_o = \frac{n_t\, 2/(n_o+n_1)}{n_t\, 1/n_o} = \frac{2\, n_o}{n_o+n_1},$$

where $n_o = n_i \exp[(E_F-E_i)/kT]$ and $n_1 = n_i \exp[(E_T-E_i)/kT]$. Furthermore, $n_1/n_o = \exp[(E_T-E_F)/kT] \gg 1$ for $E_T-E_F > 0.08V$ so that

$$(2\text{-}13) \quad \tau/\tau_o = 2n_o/n_1 = a/c \quad \text{(for large } n_t)$$

allowing eqn. (2-10) to be approximated by

$$(2\text{-}14) \quad \tau/\tau_o = \frac{1 + n_t\, 2/n_1}{1 + n_t\, 1/n_o}$$

for most cases. The relative lifetime will thus decrease for $n_1 > 2n_o$ and increase for the reverse. The trap levels E_T, for which these equations were derived are just the levels introduced near the band gap edges by the dopants. Hence $E_T > E_F$ for all but heavily doped materials, and τ/τ_o can be expected to decrease with increasing n_t. For $n_t \ll n_o$, the recombination rate is limited by the availability of holes, so that $\tau = \tau_o$, constant. The lifetime first begins to feel the effect of the increasing carrier density as $n_t = n_o$, then continues to decrease to $a/c = 2n_o/n_1$ as n_t approaches n_1. As n_t increases past n_o, the supply of holes becomes equal to the supply of electrons allowing the recombination rate to increase rapidly until n_t approaches n_1, when the supply of traps begins to aturate. Then τ again becomes constant at the new value of $(2\, n_o\, \tau_o)/n_1$.

The curves in Fig.2.7 were calculated for $n_o = 10^{14}/cc$ for two

different trap levels corresponding to phosphorus (0.045V below E_c) and sulfur (0.18V below E_c) donor levels. The knee of the curve corresponds approximately to the doping level of 10^{14}/cc, while the magnitude of the decrease (and the range of effective carrier densities) depend on the magnitude of the difference between the trap energy and the Fermi level. Hence greater decreases in τ are predicted for traps located closer to the conduction band and lifetime decreases will be observed at lower carrier concentrations in lightly doped materials. Raising the doping level thus shifts the knee of the curve to the right and decreases the maximum change in τ.

Enhanced recombination at centers close to the band edge (traps) is very interesting since the most efficient recombination centers are usually found at midgap energies. However this efficiency results from the balance in supply of both carrier types due to the midgap location, and for that very reason, the above treatment predicts little change in τ with increasing n_t for such centers [22]. Although these results were obtained for impurity centers, they should also be valid for traps associated with crystal defects having energies above E_F.

Miller et al [24] suggest another effect of high carrier density. At sufficiently high carrier concentrations, a highly conductive plasma can form within the depletion layer which prevents the built-in field from penetrating past the plasma boundary. In this case the plasma boundary and the surface of the generation volume coincide. Charge collection occurs only at the plasma surface, gradually eroding the plasma over a duration of several nsec. During this time the plasma is held together by its internal attractive forces, such that the excess charge within the generation volume can be thought of as existing in the absence of an external field.

The combination of this plasma effect with the lifetime decrease for high carrier concentrations can thus result in a substantially reduced collection efficiency within the depletion layer of a Schottky diode. For the P levels in Fig.2.7, a relative decrease in lifetime in excess of four orders of magnitude is predicted for $n_t > 10^{19}$/cc. For a material with τ_0 near 1 μsec, confinement of the carriers to the generation volume for 10 nsec under these conditions should result in significant recombination. Because excess carrier concentration increases with decreasing beam energy, this effect will be more pronounced at lower beam energies.

Variations of the beam energy can also be used to estimate defect depth within the depletion layer. For the case of an Al Schottky barrier on p-type Si, electrons in the depletion layer will drift toward the surface while holes will drift into the bulk. When the incident electron range R is less than the width of the depletion layer, $R < x_d$, primarily excess holes will be found between R and x_d. For a defect in this region, $R < x < x_d$, recombination of the excess holes will be slight due to the scarcity of available free electrons and the defect will be imaged only weakly. When R is increased to the defect depth, free electrons become available for recombination and the defect will be imaged clearly. The resolution of this technique depends both on the defect depth (due to the tail on the $\lambda(y)$ curve in Fig.(2.5), and the depletion layer width. The technique becomes less accurate with greater depth, and in general is limited to between 0.5 and 1 μm.

Very little theoretical analysis is available for $R < x_d$, probably because 1-10 Ohm-cm material is studied at beam energies in excess of 10 KeV; i.e. in most practical applications the generation volume almost always exceeds x_d.

When the generation volume penetrates beyond the depletion layer (R >
x_d), the excess carrier concentration decreases exponentially beyond R and
the collection efficiency can be given by (2-15) where L is the bulk

$$(2-15) \qquad e_c = \int_0^{x_d} N(x) \, dx + \int_{x_d}^R N(x) \exp[(x_d-x)/L]dx \quad [2]$$

diffusion length. The first integral represents the depletion layer
contribution and the second accounts for the diffusion region beyond x_d.
Fig.2.8 shows e_c as a function of x_d/R for three values of L/R, computed
from the above expression [2,25]. For electron ranges
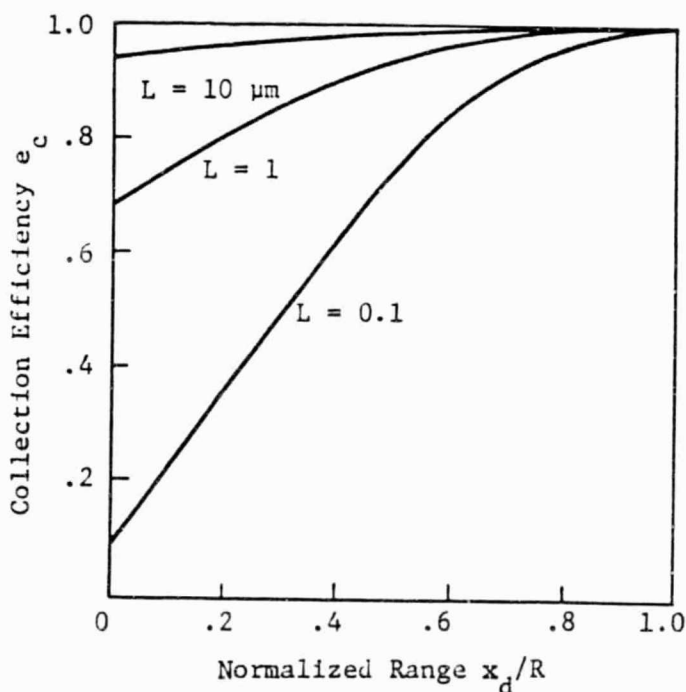
Fig. 2.8.

Charge collection effi-
ciency as a function of
primary electron range,
for three different
values of the bulk dif-
fusion length L. Range
is normalized to the
depletion layer width
x_d [2].

R >> x_d, e_c can range from near zero for short diffusion lengths (L/R << 1)
to near 1 for long diffusion lengths (L/R >> 1). e_c approaches 1 for all
values of L when the range approaches the depletion layer width. This
result is valid only for low carrier densities, low concentrations of point
defects and the absence of localized defects such as dislocations.

II.D.2. ANALYTICAL MODELS

For the case $R \gg x_d$, Donolato [26] has provided an analytic expression for the contrast and resolution that can be expected for the specific cases of 1) a point defect and 2) a dislocation perpendicular to the surface. In this treatment Donolato approximated the generation volume by a uniform sphere tangent to the surface, and accounted for charge collected by the depletion layer by assigning an infinite recombination velocity to the surface. Carrier concentration profiles were calculated both for a perfect crystal and with the generation volume centered on a point defect (Fig.2.9).
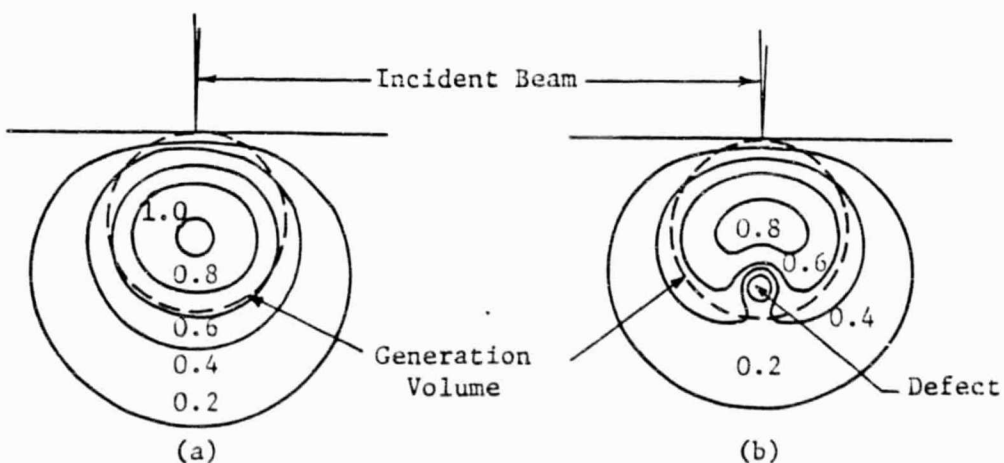
Fig. 2.9. Excess carrier isoconcentration profiles for a beam (a) incident on a perfect crystal, and (b) centered over a point defect located at R/1.2 below the surface [26].

Fig 2.9b shows how the presence of a point defect at R/1.2 in the generation volume strongly affects the carrier concentration in its immediate vicinity. In connection with this figure it is useful to distinguish between the generation volume and isoconcentration curves of

hole-electron pairs. The boundary of the generation volume defines the region within which excess carriers are generated by the incident beam. Beyond this point the excess carriers move according to diffusion laws, but no more excess pairs are formed. Thus excess carrier concentration exists at significant levels at up to twice the electron range.

Assuming low levels of carrier injection, contrast profiles $i*(y,R)$ = $I*(y,R)/I_0(R)$ were calculated as a function of the interrogating beam position y and the incident electron range R. I* denotes the recombination current to the defect (to be subtracted from the total collected current) and I_0 is the collected current in the defect-free crystal. Fig.2.10 shows
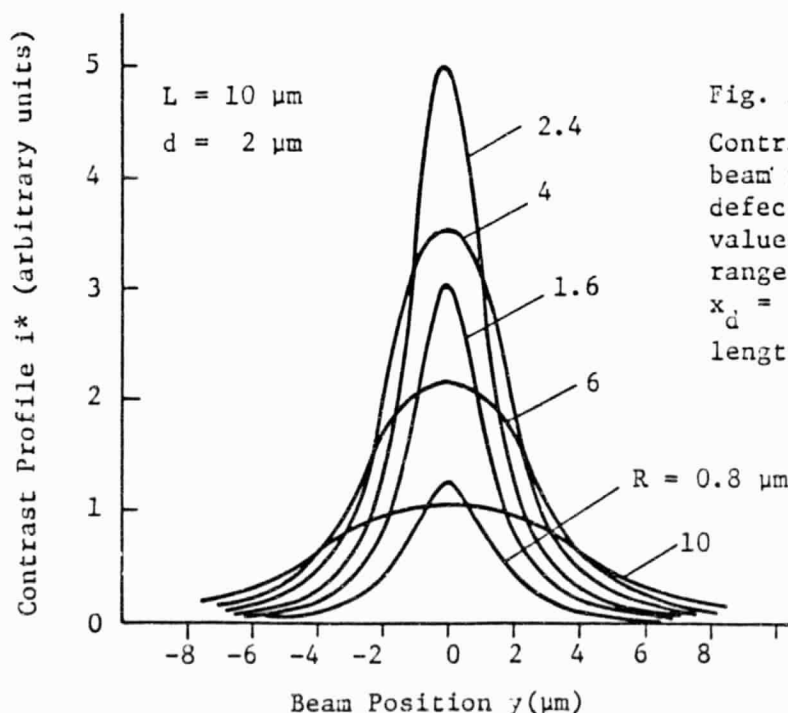
Fig. 2.10.

Contrast as a function of beam position near a point defect for six different values of primary electron range R. Defect depth x_d = 2 μm, bulk diffusion length L = 10 μm [26].

the contrast profiles [26] for a point defect 2 μm below the surface for several different electron ranges. Maximum contrast occurs at R = d, where d is the defect depth, and the half-width is approximately equal to the generation volume diameter (rather than to L as might be expected). These
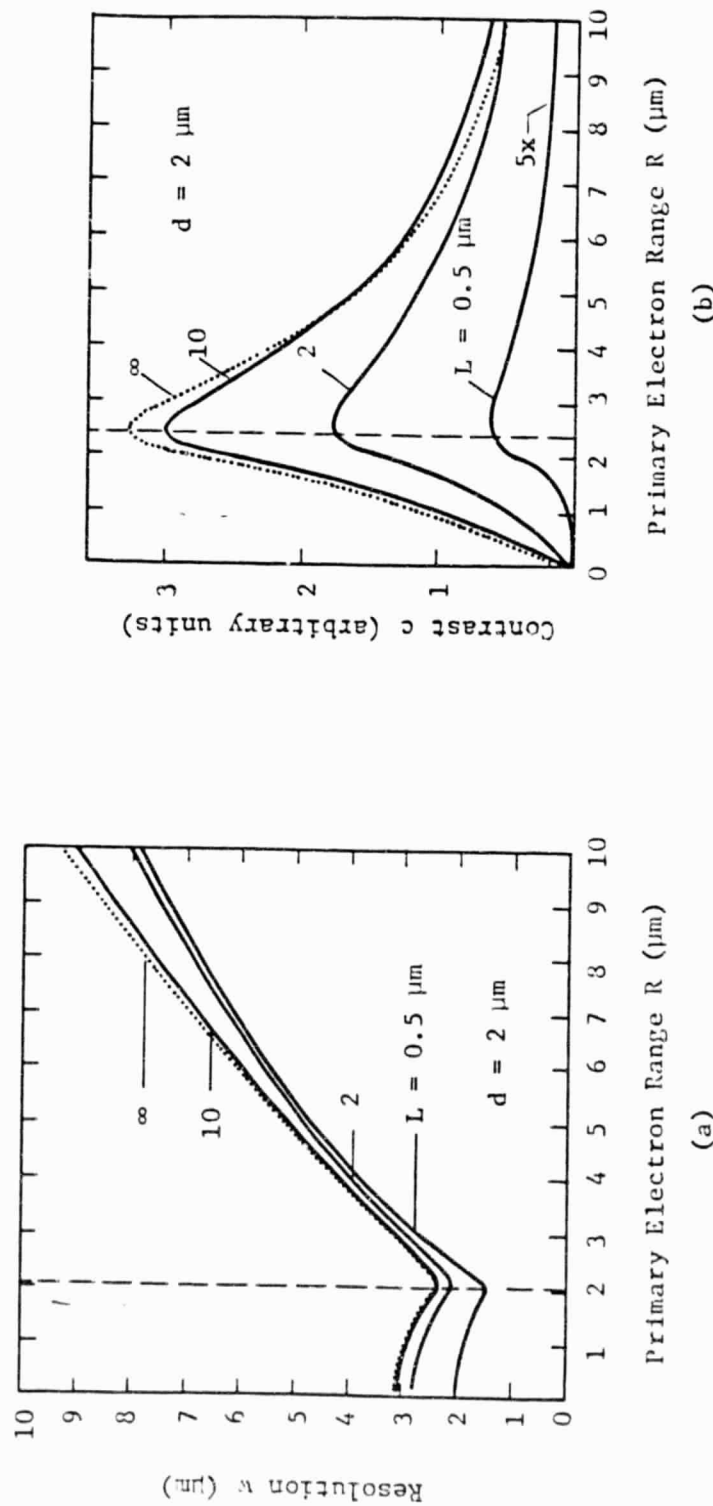
Fig. 2.11. Resolution (a) and contrast (b) of a point defect 2 μm below the surface as a function of primary electron range, for four different values of the bulk diffusion length L [26]. Note the small difference between the cases L = 10 μm and L = ∞.

dependencies and their relative insensitivity to L are illustrated in Fig.2.11. Fig.2.11a and 2.11b show contrast, c(R), and resolution (half-width), w(R), vs. R for several different values of the bulk diffusion length, including the limiting case of L = ∞. Increasing diffusion length has only a small effect on resolution, but does enhance the contrast; increases beyond 10 μm have vanishingly small effects. Fig.2.12 showing both the contrast and resolution for the limiting case of L = ∞ is thus appropriate for solar cells with conversion efficiencies greater than 10% (L > 10 μm).
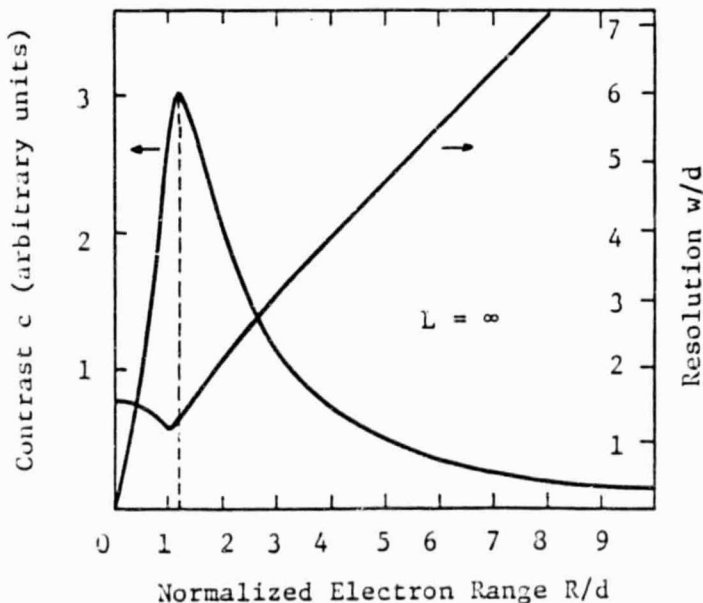
Fig. 2.12.

Contrast and resolution for the limiting case of L = ∞; scales normalized to defect depth [26].

The scales are normalized with respect to defect depth and electron range. Best contrast occurs at R/d = 1.2 and the best resolution at R/d = 1.04 [26]. Hence the best resolution for point defects is obtained at nearly the same beam energy (range) as the optimum contrast. Donolato notes that although the contrast degenerates rapidly as R/d deviates from 1.2, the resolution is affected only slightly for R/d < 1.04 and w(R) = R for R /d >

1.04. Therefore in the first approximation, for point defects w = d for R < d and w = R for R > d. The resolution is determined by the point defect depth or the generation volume diameter, whichever is larger, and is only a weak function of the bulk diffusion length.

Physical insight to these results is gained by considering the recombination process at the point defect. Denoting the lateral separation between the beam axis and the defect by y, the contrast depends upon the magnitude of the recombination current $I*(y,R)$ at y = 0, while the resolution is determined by the value of y for which $I*(y,R)$ falls below 0.5 of its peak value. The magnitude of I* is proportional to the concentration of carrier pairs N at the defect so that $I*(.5)$ will occur when the defect is at the 0.5 isoconcentration surface around the generation volume (which approximately coincides with the generation volume as shown in Fig.(2.9). In approximate terms, a defect will be imaged when it is in "contact" with the generation volume, since only there is the carrier density sufficient to cause appreciable recombination. Thus a defect at R/d > 1.2 will have an image width w = R (see Fig.2.13a and 2.13b). For point defects at R/d < 1.2, the carrier density at the defect is given by $N(s) = [exp(-s/L)]/s^2$, where s is the separation between the edge of the generation volume and the defect (Fig.2.13c) and L is the bulk diffusion length. The $1/s^2$ factor accounts for the decrease in carrier density due to spherical spreading. $I*(.5)$ then occurs at $exp[-s/L] = s^2$, which corresponds to y = d/2, or an image width w = d. The rapid decrease in contrast as R/d vanishes results from the decrease in carrier density with separation of the point defect from the generation volume. As R/d becomes large the generation volume becomes much larger than the volume from which the recombination current is drawn, increasing I_o while I*
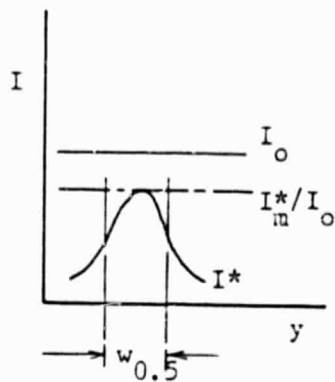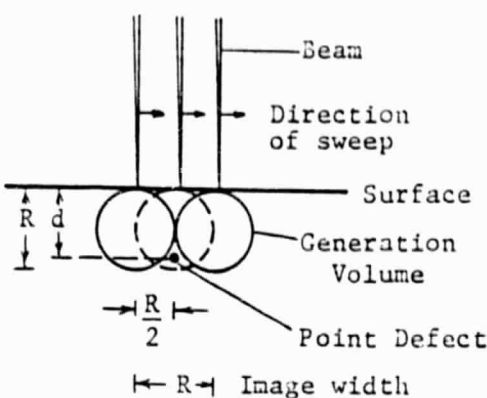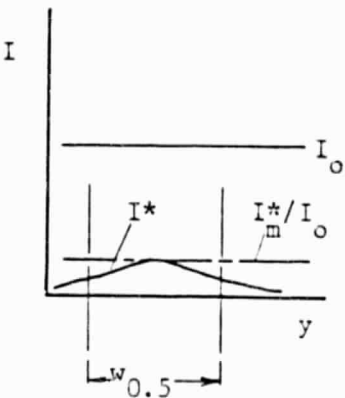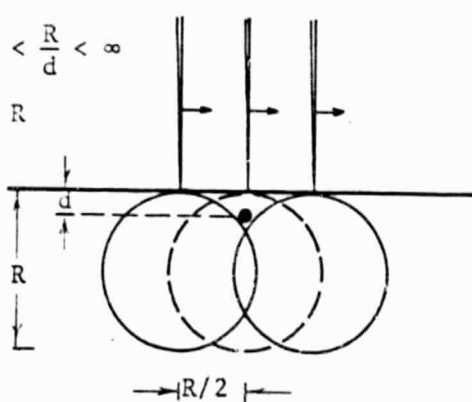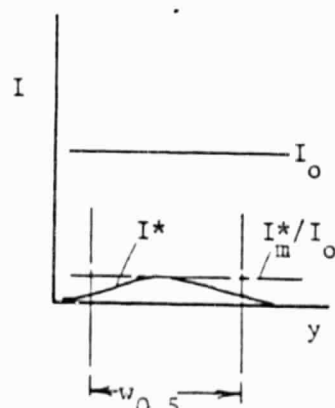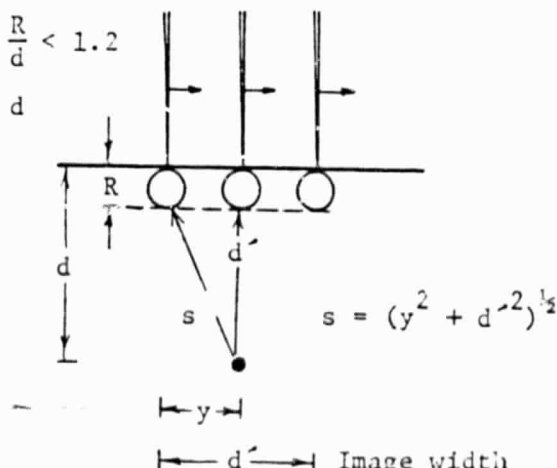
Fig. 2.13. Contrast (I_m^*/I_o) and resolution ($w_{0.5}$) for three ranges
of R/d. The graphs indicate the relationships between
the various currents.

remains constant. Hence the contrast is reduced due to a relative decrease in I*.

Donolato also addresses the resolution with which the defect depth can be determined. Maximum contrast is observed when the defect is at d = R/1.2. But $R = a E_b^b = 1.2d$ implies that

(2-16) $\ln E = (\ln 1.2/a)/B + (\ln d)/B$

i.e. the beam energy at maximum contrast is proportional to the defect depth when graphed on log-log scales. The first term is the y-intercept = 2.43 and 1/B = 0.57 is the slope of the line. Fig.2.14 shows this relationship (solid line) together with the envelope of energies that produce contrast levels greater than 80% of maximum (dotted lines).
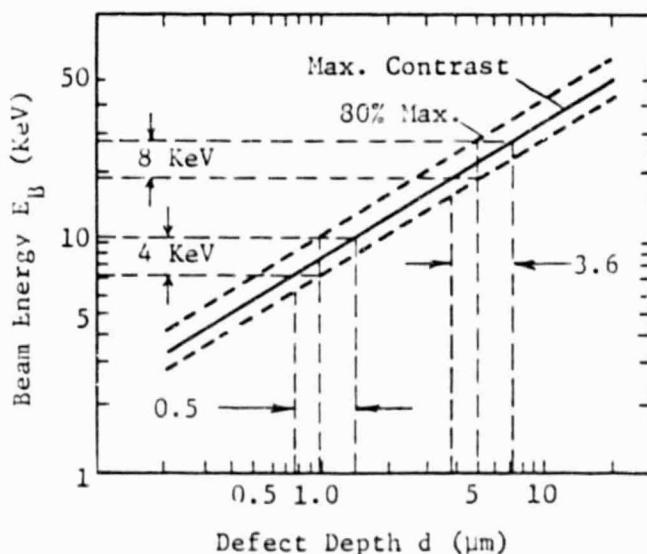
Fig. 2.14.

Defect depth resolution, assuming discrimination of a 20% drop in contrast. Resolution worsens rapidly with depth [26].

Supposing that one can detect a 20% reduction in contrast, the depth resolution of the defect will be set by the upper and lower depths at which a 20% reduction in contrast occurs. For a defect at 1 μm, we will be uncertain of its position by about 0.5 μm, while for a defect at 5 μm the

uncertainty will be about 3.6 μm, i.e. the depth resolution deteriorates rapidly with depth. This does not apply to defects within the depletion layer as discussed above.

By treating a dislocation as a string of point defects, Donolato [27] also computed contrast profiles for a dislocation perpendicular to the surface (Fig.2.15) and found that both contrast and resolution for the dislocation are maximized at the lowest beam energy (shallowest range) and degrade as the beam energy increases.
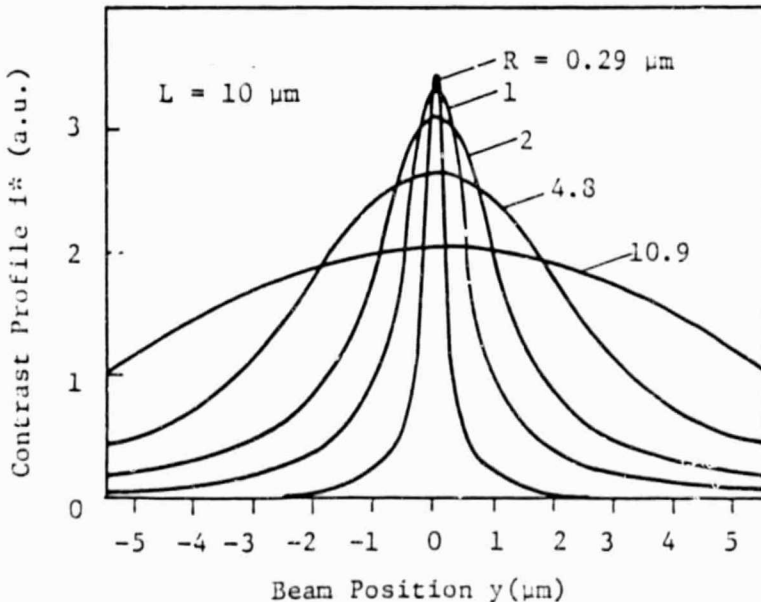
Fig. 2.15. Contrast as a function of beam position near a dislocation perpendicular to the surface for five different values of the primary electron range R [27].

This is illustrated in Fig.2.16a and 2.16b, which show the contrast and resolution of a dislocation as a function of electron range. These curves compare qualitatively with those in Fig.2.11 if only those ranges greater than the defect depth, i.e. to the right of the vertical dotted line, are
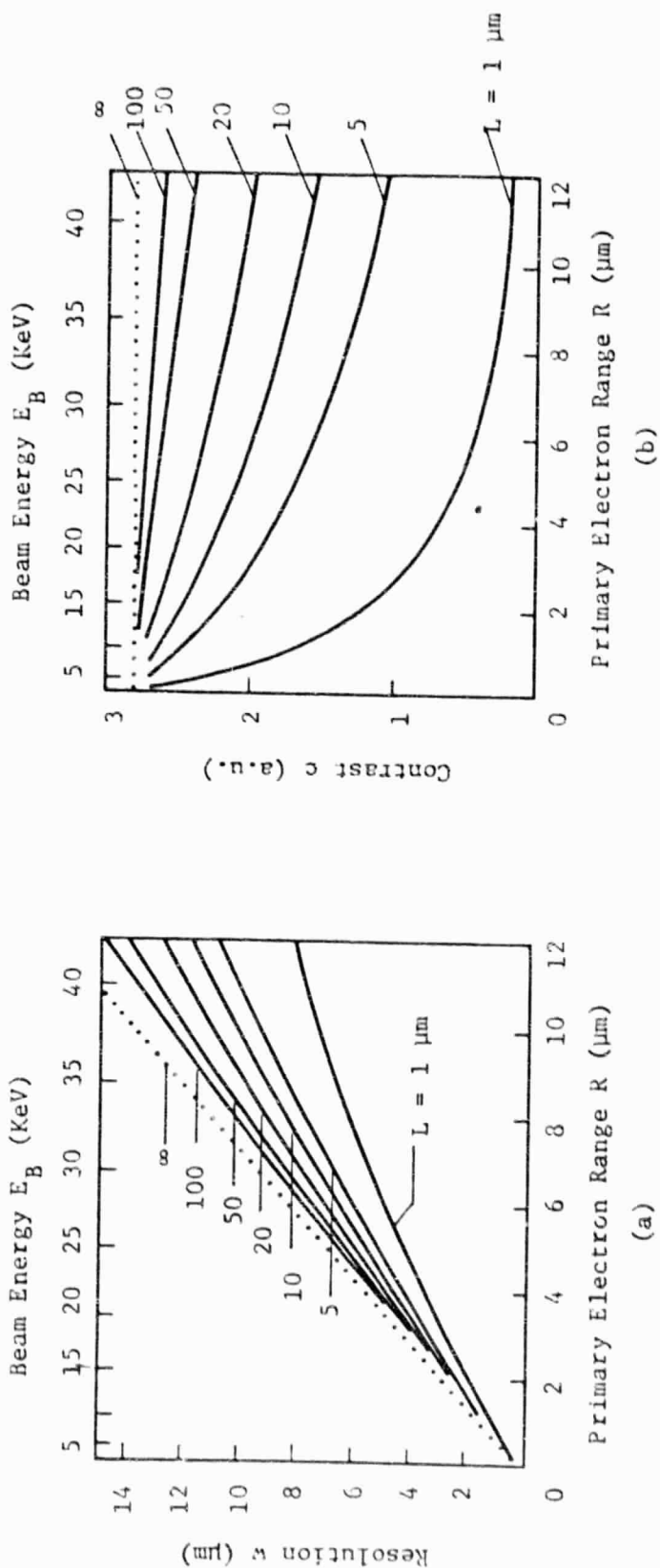
Fig. 2.16. Resolution (a) and contrast (b) of a dislocation perpendicular to the surface as a function of primary electron range, for seven different values of bulk diffusion length [27].

considered. Because dislocations are two-dimensional defects, the diffusion length L has more influence on resolution than in the case of a point defect. In the limiting case, $L = \infty$, uniformly good contrast is obtained for all beam energies.

Donolato suggests that these differences provide a method by which point defects can be distinguished from vertical dislocations. Variation of the beam energy will produce a drop in contrast for a point defect, while contrast for a dislocation will tend to remain strong.

Finally, Marek [28] modeled a grain boundary perpendicular to the surface by a planar array of point defects, using the methods introduced by Donolato. The generation volume was treated as a uniform sphere tangent to the surface, with diameter large in comparison to the depletion layer width $(R > x_d)$. Electric fields at both the depletion layer and the grain boundary were taken into account by setting the recombination velocity equal to infinity in each case. The material around the grain boundary was assumed to be homogeneous and the diffusion length L was assumed to be spatially invariant.

Both contrast and resolution were found to have a strong dependence on L, a striking result when compared to the relative insensitivity to L of the contrast and resolution exhibited by images of point defects and vertical dislocations described above. Marek's results for contrast [28] are shown in Fig.2.17a and 2.17b. For $L > R$, the contrast increases with beam energy, while for very short diffusion lengths the contrast reaches a peak at the beam energy for which $R = L$ and decreases for greater energies. The peak contrast is lower for smaller values of L, hence in accordance with observation, poor contrast is predicted in materials with short diffusion lengths. Resolution (half-width) as a function of beam energy is
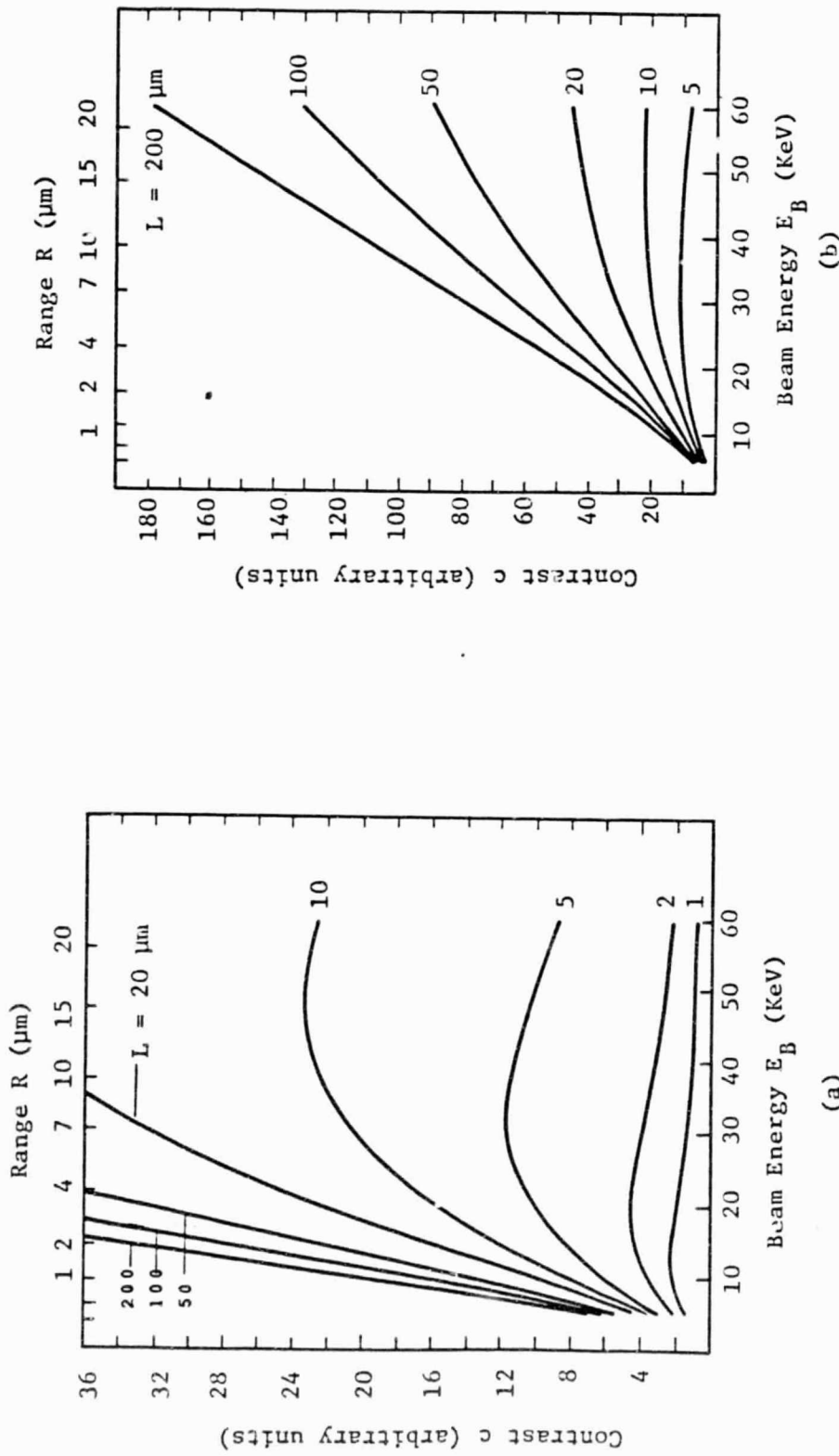
Fig. 2.17. Contrast of a grain boundary as a function of beam energy, a) for short diffusion lengths, b) for long diffusion lengths. Contrast for grain boundaries is strongly dependent upon bulk diffusion length [23].

shown in Fig.2.18. The strong dependence of the resolution on the diffusion length provides a direct method for measuring L.

Marek's predictions were confirmed to within 2% by EBIC linescans across a vertical grain boundary in a solar cell. The calculated values are compared with a linescan across a boundary separating materials having different values of L in Fig.2.19. This close agreement between theory and experiment could only be obtained by using a value for the electron range R which was twice that reported by Everhart and Hoff, conceivably because of the overestimation of the recombination velocity at the boundary.

A physical understanding of the influence of diffusion length on contrast and resolution can be gained by simply considering the spatial extent of point, line and plane defects. If a given point defect is capable of sustaining a maximum recombination rate U_m, the recombination current to the defect will grow with the supply of carriers until U_m is reached, and then will remain constant. For a constant carrier concentration far from the defect, the quantity of available carriers will grow with $(4 \pi L^3)/3$, the spherical volume of radius L around the defect, so that the recombination current (and therefore the contrast) will saturate quickly with increasing L. Although increasing L allows carriers to reach the defect from a more distant generation volume, the image width is not strongly affected because the carrier concentration decreases with the inverse square of the distance to the generation volume, balancing the effect. These results were illustrated in Fig.2.11. Visualizing a dislocation perpendicular to the surface as a linear array of point defects, the quantity of carriers available for recombination will grow with (πhL^2), the cylindrical volume about the dislocation of radius L, where h is the average separation of point defects in the line. In

Range R (μm)

1 2 4 7 10 15 20
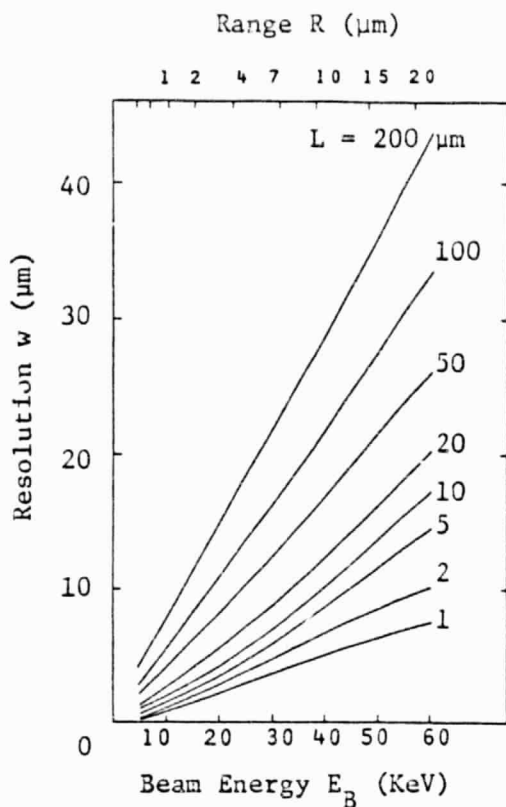
Fig. 2.18.

Resolution of a grain boundary
as a function of beam energy,
for eight different values of
bulk diffusion length [28].

Beam Energy E_B (KeV)

Beam Position y (μm)

-40   -30   -20   -10   0   10   20   30   40

L = 19.5 μm

L = 65 μm
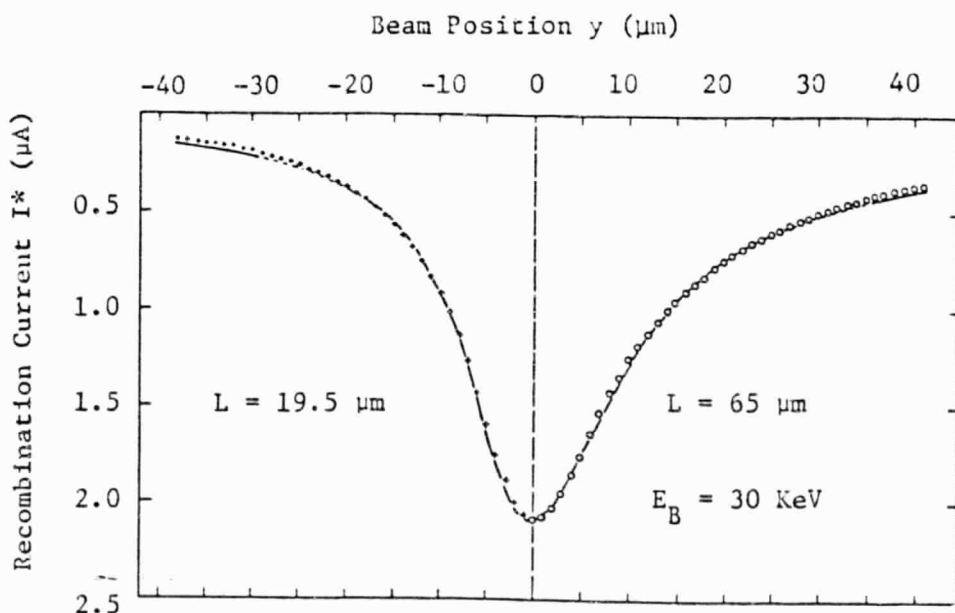
E_B = 30 KeV

Fig. 2.19. Comparison of calculated and measured recom-
bination current as a function of beam posi-
tion across a grain boundary at E_B = 30 KeV
[28].

addition, more recombination centers become accessible to the carriers with increasing L, so that the recombination current, and thus the contrast, will not saturate as quickly as for the point defect. The larger number of recombination centers available at a given distance from the generation volume will also cause the resolution to degrade more quickly than for the point defect, as shown in Fig.2.16. Similarly, viewing a grain boundary as a two-dimensional array of point defects, the quantity of carriers available for recombination grows only with $2h^2L$, where h^2L is the volume normal to a square area of side h about each point defect. However the number of recombination centers within reach of the generation volume grows approximately with L^2. Hence saturation of the recombination centers occurs very slowly, and contrast increases rapidly with L. Image width also increases rapidly with L, because the decrease in carrier density with distance from the generation volume is offset by a similar increase in the number of recombination centers able to capture. Thus the influence of L on the image is due primarily to geometric factors.

III. HYDROGENATION

The term hydrogenation refers to processes in which a Si specimen is immersed in molecular or ionized hydrogen (H) at elevated temperatures, typically between 200°C and 400°C. Reduction of the electrical activity (recombination rate) caused by defects in the specimen after hydrogenation is referred to as hydrogen passivation. Passivation is usually acheived with plasma hydrogenation [29,30], but first Pankove et al [31] and more recently Lam [32] observed measurable effects also with molecular hydrogen (H_2). Plasmas used are generated at pressures on the order of 1 Torr (1 mm Hg) by ionization of H_2 through one of several methods including the following:

(1) photon excitation by a mercury vapor lamp

   discharge,

(2) electromagnetic excitation by an R-F coil

   wound external to the tube containing the

   hydrogen,

(3) R-F excitation which is either inductively

   or capacitively coupled into the system.

An example of the apparatus used for R-F excitation is shown in Fig.3.1. The plasma parameters are generally not specified, and are probably not known. The characterization of a plasma is a difficult and an entire field of study, plasma diagnostics, is devoted to the task [33]. The electron density and temperature within the plasma can be measured with an electrostatic (Langmuir) probe [34], but that provides little information about the composition of the plasma itself. Production of the plasma by one of the above methods probably does not ionize the gas completely. If

41

the molecular hydrogen is initially pure, at least the four following components are likely to be present: H_2, H, H^+, H_2^+. The relative
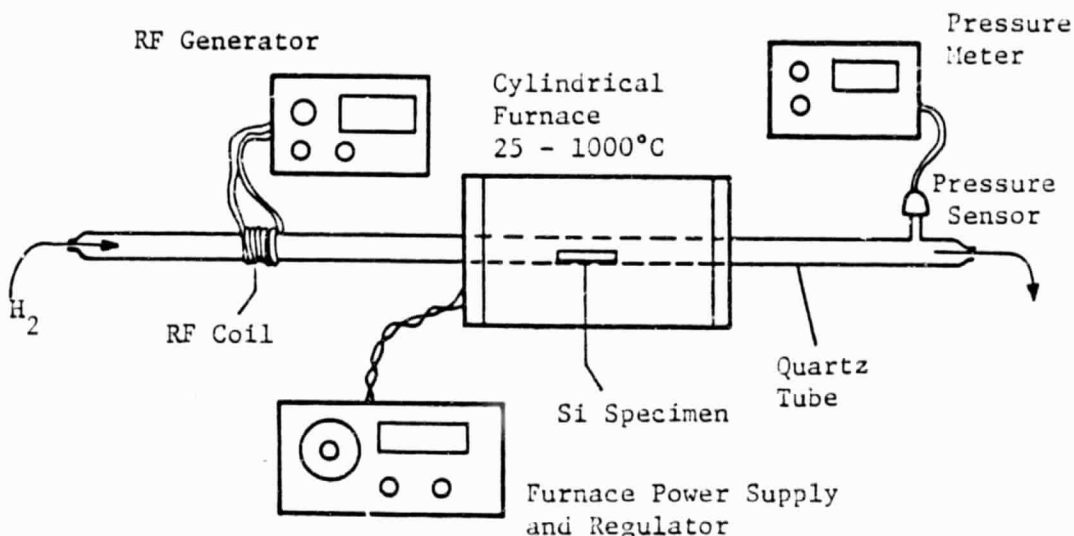
Fig. 3.1. An example of equipment used to hydrogenate a
Si specimen.

concentrations of each of these is likely to vary with the method and intensity of excitation, and the initial pressure of H_2. Which of these components is responsible for the reduced recombination rates is not known, but the monatomic species are more likely since H_2 must dissociate before entering the specimen.

Pankove et al [31] were the first to report the effects of hydrogenation on crystalline Si. In their experiment an array of rather leaky p-n junctions was exposed to a glow-discharge at $550^{\circ}C$ and then cooled in the discharge to room temperature. Measurement of the reverse current characteristics of the diodes showed that an initially high leakage current had been reduced by about three orders of magnitude by the hydrogenation, and the reverse breakdown was substantially sharpened (Fig.

3.2). When the diodes were dehydrogenated by slow heating in a vacuum to a
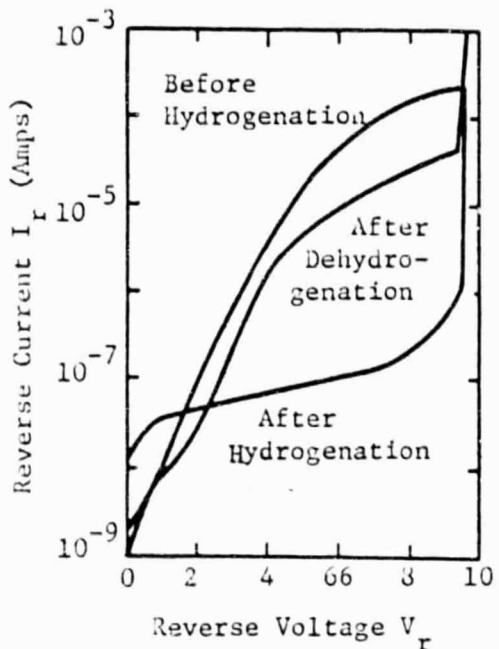
Fig. 3.2.

Reverse current characteristics of
a p-n junction before hydrogenation,
after hydrogenation, and after
dehydrogenation [31].

temperature of 550°C, the reverse current characteristics returned to near
their original values. Exposure of untreated diodes to H_2 also showed a
reduction in the leakage current, but only by a factor of five. When these
diodes were then exposed to the plasma, the entire three orders of
magnitude reduction was again observed.

Pankove et al [31] suggested that the high leakage current was due to
the presence of "dangling bonds" in the junction region and that during
hydrogenation, monatomic hydrogen tied up the dangling bonds which
previously acted as recombination centers. The term "dangling bond" refers
to a partially filled covalent bond in the diamond crystal lattice.
Electrons within the s-p hybrid bonds characteristic of the tetrahedrally
coordinated lattice are shared by specific pairs of nearest neighbor atoms.
The bond is well-localized in space and highly directional. Removal of one

of the atoms participating in the bond raises the energy of the other atom due to the unpaired electron in the half-empty orbital. The shape of the orbital changes some as the unpaired electron spends more time next to the parent nucleus, but it remains directional and occupies the same general region of space. This is the dangling bond.

The atom can lower its energy by forming another bond, and is therefore expected to attract diffusing impurity atoms (such as atomic H) with single outer electrons. In the absence of such atoms, free electrons are pulled into the empty orbital. The atom is then electrically charged, however, and the energy reduction achieved by free electron capture is small -- some fraction of the bandgap energy --- and the electron is not tightly bound. When both free holes and electrons are present, the lightly bound electron attracts a free hole and annihilation (recombination) occurs, locally reducing the number of free carriers. After recombination, the site is available to capture another electron and repeat the cycle. Alternately a recombination center can provide an intermediate state by which a carrier can more easily transit the forbidden gap. Since the probability of an electron acquiring an energy E is proportional to the Boltzmann factor $\exp(-E/kT)$, the most efficient recombination centers are located at midgap, and can increase the probability of immobile carriers crossing the gap (carrier generation) by nearly 10 orders of magnitude.

In a defect-free p-n junction under reverse bias, the leakage current is due to (1) minority carriers from outside the depletion layer (neutral region) diffusing through the junction, and (2) the flux out of the junction of carriers generated within the depletion layer (Fig.3.3). Carrier generation in a defect-free crystal is insignificant since the bound carrier must acquire E_g to become mobile. Thus the reverse current
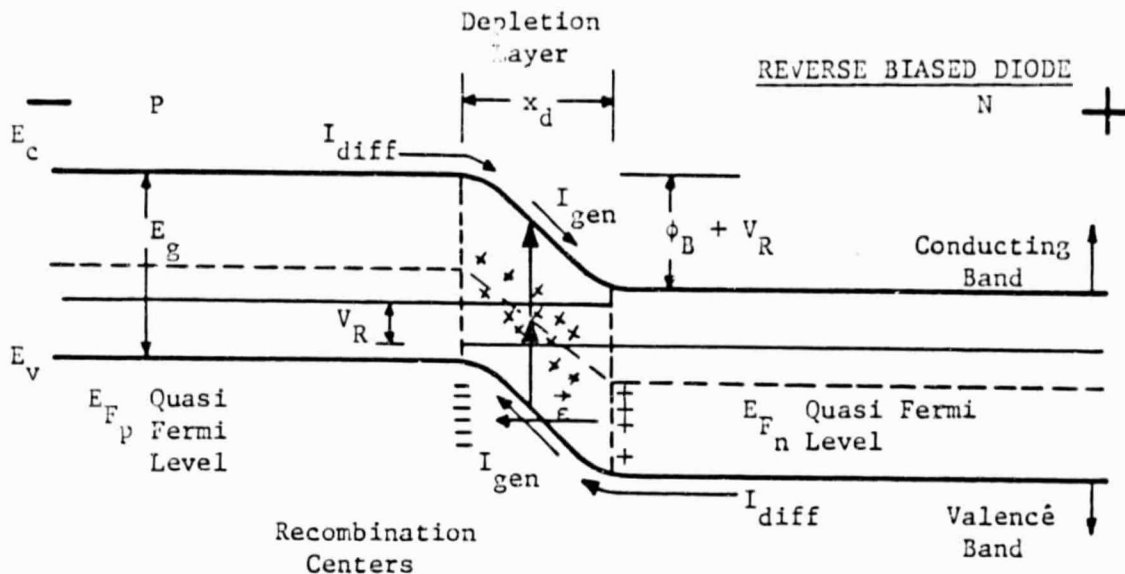
Fig. 3.3. Diagrammatic representation of leakage current (I_r) in a p-n junction augmented by the presence of recombination centers within the depletion layer, with midgap energies.

(leakage current) will result only from minority carrier diffusion through the junction and will be independent of the applied reverse voltage. When defects are present, the generation of carrier pairs within the depletion layer greatly increases. The number of pairs generated will be proportional to the Boltzmann factor multiplied by the concentration of centers and the depletion layer volume. Increasing the reverse voltage increases the depletion layer volume by increasing the depletion layer width x_d, and thus increases the leakage current by including more recombination centers. Hence the presence of defects should produce a voltage dependence in the leakage current. Pankove et al suggested that if this model is correct, exposure of the junction to H should passify the dangling bonds associated with the defects, removing the voltage dependence of the leakage current and reducing its magnitude, as shown in their data (Fig.3.2).

Polycrystalline Si (polysilicon) contains numerous defects including grain boundaries, twin boundaries and dislocations. A large number of dangling bonds are presumably associated with these defects. Since polycrystalline solar cells perform in general much less efficiently than single crystalline cells, a natural extension to the work of Pankove et al [31] was to examine the effects of hydrogen on the electrical properties of grain boundaries. Seager and Ginley [29] measured the potential drop across grain boundaries before and after hydrogenation. A small Si bar (1 X 0.1 X 0.03 cm) was cut out of polysilicon having an average grain size between 0.2 and 0.5 mm. Grain boundaries were normal to the surface, usually extending through the bar. A fine wire voltage probe was drawn lengthwise along the bar during application of a steady-state current to detect voltage drops across the grain boundaries. Grain boundary transconductances were calculated from these measurements. The bar was subjected to a sequence of annealing steps ranging from 300°-600°C (usually alternating between the higher and lower extremes), in vacuum (best: 3 X 10^{-6} Torr), H_2, O_2 and plasma at several pressures. Immersion of the bar in a hydrogen plasma at 300°-400°C for about three hours increased the grain boundary transconductance by about one order of magnitude, while annealing the bar near 600°C in a vacuum for a somewhat shorter time restored the transconductance to approximately its original value. Annealing the hydrogenated bar in H_2 at 337°C lowered the transconductance slightly. Annealing the hydrogenated bar in O_2 reduced the transconductance about the same amount as annealing in a vacuum. The authors concluded that the hydrogenation-dehydrogenation cycle could be performed indefinitely and that molecular hydrogen had no effect. They furthermore observed that hydrogenation produced no measureable changes in

the conductivity of bulk Si.

Benton et al [30] demonstrated that hydrogenation passivates point defects in bulk Si. Defect concentrations were measured both by deep-level transient spectroscopy (DLTS) and thermally stimulated capacitance scans (TSCAP). 5 Ohm-cm Si (float-zone, phosphorus doped) which had been laser melted to a depth of 1.2 µm, was found to contain point defect states in concentrations of about 10^{14}/cc (1 µm deep) increasing to about 10^{16}/cc near the surface. Observed energy levels of these defects were 0.33 eV and 0.19 eV from the band edge. Exposure to a hydrogen plasma at 200°C for times as short as 10 minutes was found sufficient to reduce the concentrations of these defects below observable levels. Dehydrogenation in a 2 mTorr vacuum for 1 hour at 400°C restored the trap concentration to about half of its initial level.

An interesting study by Makino and Nakamura [35] investigated the effects of hydrogenation on polysilicon as a function of doping concentration. Specimens were 0.5 µm thick chemically vapor deposited (CVD) films implanted with boron (B) or phosphorus (P) in concentrations ranging from 10^{16}-10^{19}/cc. Resistivity was observed to decrease from one to four orders of magnitude in the doping regime 10^{17}-10^{19}/cc, while only small effects were observed for doping levels greater than 10^{19}/cc or less than 10^{16}/cc (Fig.3.4). The effect was much more pronounced for P doping.

The authors explain their results in terms of a model proposed by Seto [36] for grain boundary trapping of carriers. Here, N_t traps per unit area of grain boundary are available to capture free carriers from the bulk. For a bulk doping concentration N_D (per cc) and grain diameter L_g, the boundary will capture $N_t = (2N_d \, x_d)$ majority carriers from the bulk, forming a depletion layer of width $x_d = N_t/2N_d < L_g/2$ into the grain
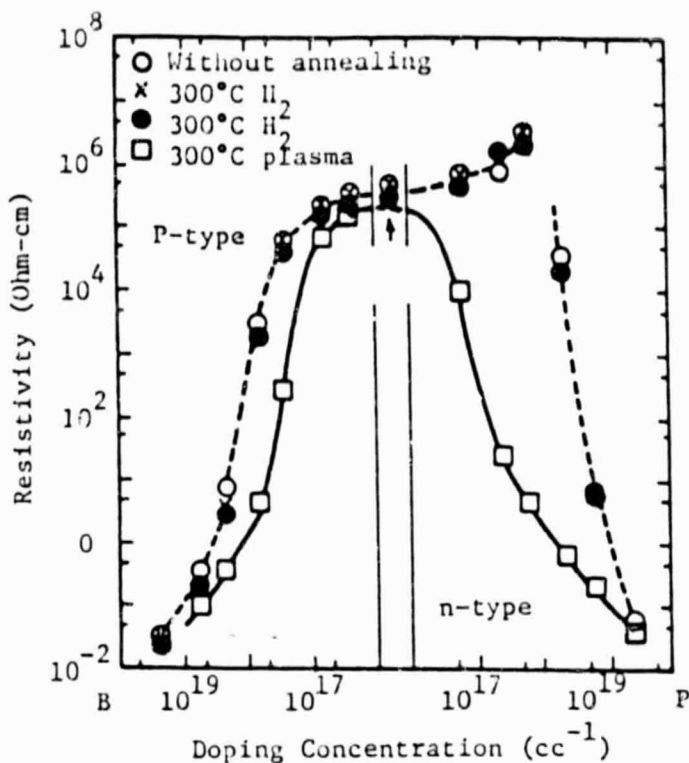
Fig. 3.4.

Resistivity at room temp-
erature vs. doping level
for CVD Silicon film,
hydrogenated and unhydro-
genated.
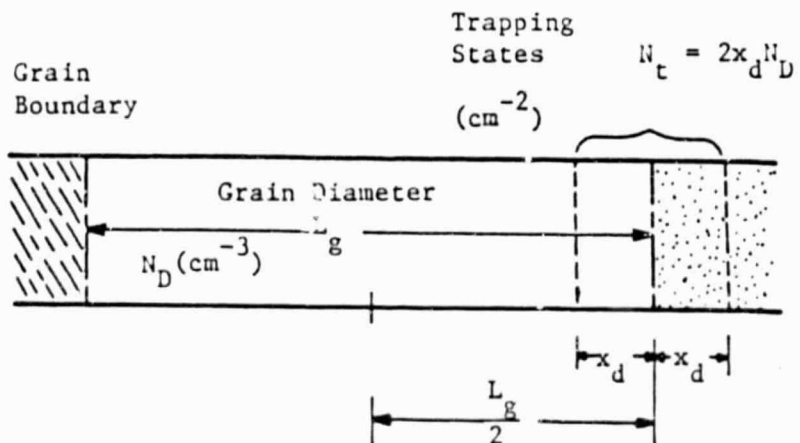
Fig. 3.5. Cross-section of a grain, illustrating the
carrier trapping model of grain boundary.

(Fig.3.5). x_d will be large for low doping levels and small for high doping levels. The trapped majority carriers form a repulsive barrier of height V_B to the remaining free majority carriers. For barrier energy E_B = ($q V_B$), the thermally generated current across the barrier is proportional to $\exp(-E_B/kT)$ and will have a minimum when E_B (and hence V_B) is at a maximum. The effective barrier height is the difference between the energy of the free carriers outside the depletion layer ($x_d/2$ away from the boundary) and E_B. Hence E_B will have a maximum when the number of free carriers in the grain is equal to $N_t/2$ (i.e., all free carriers are captured by the boundary). For 1 μm thick CVD specimens with 200-250Å grains, Seto found a minimum in the Hall mobility μ_H at a doping level of about 10^{18}/cc (Fig.3.6). This is the same minimum as would be seen for the
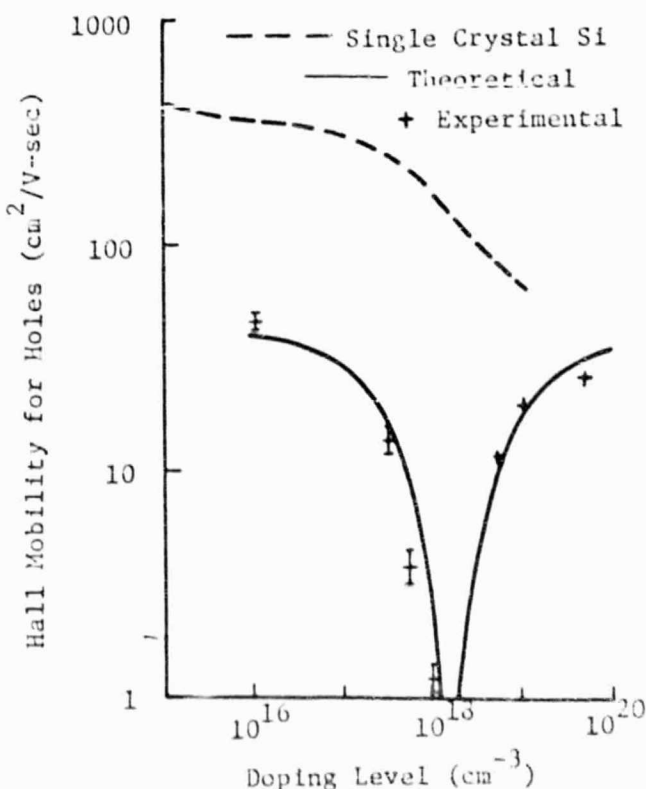
Fig. 3.6.

Hall mobility in CVD poly-crystalline film vs. doping level (both theoretical and experimental). Single crystal mobility plotted for reference.

conductivity σ since $\sigma = N_d q \mu = (N_d q \mu_H)/r$ (i.e., $\mu_H = (r\mu)$ and r is

constant if the carrier energy is constant. These measurements correspond to an average trap concentration of $N_t = 3.34 \times 10^{12}/cm^2$ (less than 1% of the surface atom density).

The results shown in Figs.3.4 and 3.6 can be explained by Seto's model if the density of states $N(E)$ is assumed to peak below midgap. Then the barriers are greater (as observed) when electrons are trapped (P-doped) than when holes are trapped (B-doped). Hydrogenation presumably eliminates the traps, freeing the trapped carriers (thus removing the barrier) and lowering the resistivity. At low doping levels the number of carriers is small, $(NL_g)/2 < N_t$, which produces a small barrier. Since the resistivity in this regime is controlled by the scarcity of carriers, removal of the barrier through hydrogenation has little effect on the resistivity. At very high doping levels ($10^{19}/cc$) the free carrier energy is nearly equal to the barrier energy such that the effective barrier height is again small. Removal of the barrier by hydrogenation increases the free carriers by an insignificant percentage and again has little effect. In the intermediate range, when the doping concentration roughly equals the trap concentration, the barrier height is large and the carrier concentration is small. Hydrogenation increases the majority carrier concentration by orders of magnitude and at the same time removes the barrier. Hence the effectiveness of hydrogenation is at a maximum.

Ast and Sullivan [37] first attempted to observe the effects of hydrogenation on Si grain boundaries in a scanning electron microscope in the EBIC mode by imaging EFG (edge-defined, film-fed grown) polysilicon ribbon before and after hydrogenation. (The structure of EFG ribbon will be described in greater detail below.) After imaging the untreated specimen, the Schottky barrier (Al = 300Å) was removed, and the specimen

was hydrogenated in a 1/2 Torr plasma for 30 minutes at 550°C. The specimen was cooled to room temperature over 1.5 hours while still in the plasma. EBIC micrographs at 21 KeV of the same region before and after hydrogenation were taken to compare the electrical activity of various defects before and after hydrogenation. Two effects were observed: 1) the ratio of collected current to injected current increased (i.e. the EBIC images after hydrogenation were brighter under similar imaging conditions); 2) the contrast of some (but not all) defects decreased noticeably. Fig.3.7 shows a region before and Fig.3.8 shows the same region after hydrogenation, with arrows indicating defects exhibiting reduced contrast after hydrogenation. Defects showing strong contrast before hydrogenation tended to still show strong contrast afterward, and only defects with initially light contrast showed marked contrast reduction. Attempts to restore contrast to its original strength by driving off the hydrogen were unsuccessful.

Seager et al [38] observed the effects of hydrogenation on grain boundaries in polysilicon (SOC Honeywell) p-n junctions with EBIC "maps" formed by scanning the specimen with a 25 KeV beam of an ISI "MINI-SEM" microscope. The junction was about 0.5 µm below the surface and parallel to it. Thin film strips of tungsten (W) were sputter deposited over the surface to serve as EBIC contacts. W was used to minimize the diffusion of the barrier metal into the Si during the elevated hydrogenation temperatures. After hydrogenation at a plasma pressure of 2 Torr for 16 hours at 350°C, contrast of nearly all grain boundaries initially observed had disappeared.

References [37] and [38] have shown that EBIC may be a useful tool for investigating the effectiveness of hydrogenation in passivating defects in

Fig. 3.7. EBIC micrograph of typical defect structure observed in unprocessed EFG ribbon.

100X

Fig. 3.8. EBIC micrograph of area shown in Fig. 3.7. after hydrogenation. Arrows indicate regions of reduced contrast.

Si. EBIC images were shown [37] to be reproducible at low (250X) magnification over several cycles of application and removal of the Al Schottky diodes. More extensive investigations require the development of greater quantitative control over the parameters affecting contrast and resolution of EBIC micrographs. Also, hydrogenation involves exposure of a specimen not only to ionized hydrogen, but also to elevated temperatures, a factor usually ignored in the literature. Since low-temperature ($< 600^{o}C$) annealing of Si has been shown [39,40] to cause such effects as alteration of the lifetime (presumably through thermal conversion of oxygen donor complexes) in 1 Ohm-cm float-zoned Si, detection of thermally induced effects during hydrogenation is also required. These formed the goals of the following experiments.

IV. EXPERIMENTAL

IV.A. EQUIPMENT

A JEOL 733 microprobe was adapted to provide and display an EBIC signal in the following manner. 1) The specimen chamber was provided with a vacuum tight coaxial feedthrough contact. 2) A special specimen holder was fabricated to contact the Al Schottky diodes and deliver the EBIC signal to the feedthrough contact. 3) The EBIC signal was amplified externally with a Keithley 427 fast current amplifier. 4) Access for input into the display intensity modulation network was provided. The 733 was

TABLE I. Relevant capabilities of the JEOL 733.

1) Beam current magnitude is measured with a Faraday cage pneumatically inserted under computer control, with an external printout.

2) Lens currents automatically adjust with magnification changes (focusing need only be done once at high magnification).

3) The magnitude of current collected along a linescan can be displayed on the CRT, with the y-axis representing the EBIC current and the x-axis representing the location of the incident beam along the scan. This feature is useful for quantifying EBIC contrast.

4) Polaroid photographs are obtained from a separate display. Beam voltage, image magnification, micron reference marker, and photograph number are all printed automatically on each photograph. A reference grid, linescan intensity curve, and cursor position can be superimposed on each photograph as well.

already equipped with the features listed in Table I. A schematic representation of the principal equipment used to produce the EBIC display is given in Fig.2.1. Fig.4.1 shows a diagram of the specimen holder.
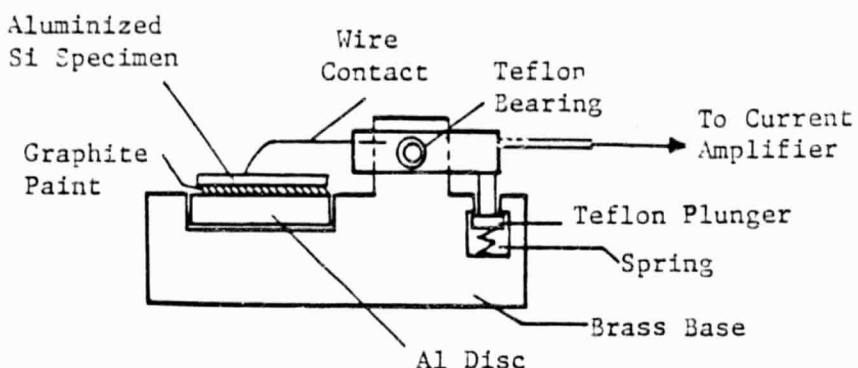
Fig. 4.1. Schematic representation of EBIC specimen
holder.

IV.B. SPECIMEN PREPARATION

The material used in this study was 205 Ohm-cm nominally undoped
p-type EFG Si ribbon produced by Mobil-Tycho. The EFG process uses a
carbon die with a thin flat central capillary submerged in the molten Si
(Fig.4.2). The melt is drawn up the capillary by surface tension to the
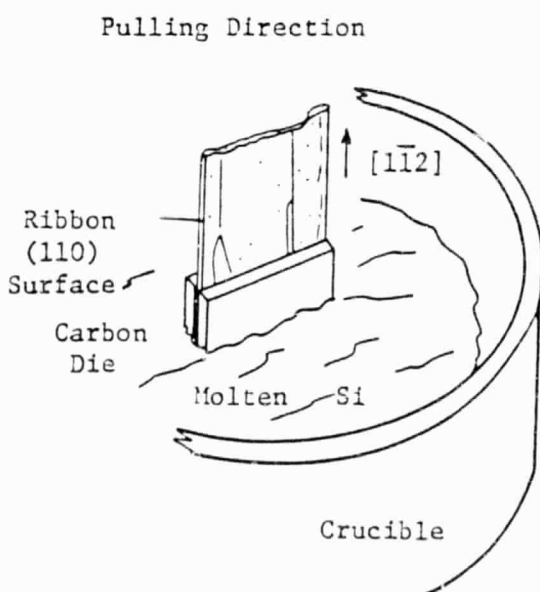
Fig. 4.2.

Production of EFG ribbon.
Carbon die with flat thin
capillary is partially sub-
merged in molten Si. Sur-
face tension draws the
liquid Si up the capillary
where it contacts the seed
crystal and is then drawn
slowly upward, gradually
cooling and crystallizing.

top of the die into contact with a seed crystal. The seed crystal is then slowly withdrawn. Heat transfer into the seed crystal and radiant cooling cause the melt immediately adjacent to the seed to crystallize allowing the seed to gradually lengthen into a ribbon. Garone et al [41] have shown that EFG ribbons always tend to orient themselves such that the flat face is a <110> plane being pulled along a {211} direction (Fig.4.2), regardless of the initial seed orientation. Defect structures tend to be grouped into relatively continuous bands separated by microtwin boundaries parallel to the pulling direction. The surface of ribbon material has a rippled appearance due to growth fluctuations, with additional surface morphology corresponding to underlying defect structures. The first step in specimen preparation is therefore mechanical grinding, using a series of successively finer SiC grits. The surface is then optically polished with Syton to remove the remaining mechanical damage (scratches) introduced by grinding. The specimen, now with a mirror finish, is cleaned with the RCA cleaning cycle given in Table II.

TABLE II. RCA cleaning cycle.

1) degreased ultrasonically for 5 min in acetone (or other organic solvent)
2) boiled in concentrated HNO_3 for 10 min,
3) rinsed carefully in deionized water,
4) boiled in H_2O : NH_4OH : H_2O_2 (7:2:1) for 10 min,
5) rinsed carefully in deionized water,
6) stored in deionized water until immediately before being vacuum deposited.

The specimen is then ready to have Al deposited on its polished surface to form the Schottky barrier. Immediately prior to vacuum deposition, the specimen is dipped for 30 seconds into a 48% hydroflouric (HF) acid solution to remove residual SiO_2. Then it is rinsed in methanol to remove

the HF, and dried with an air jet.

The specimen is taped to a stainless steel mask with a square grid of holes and placed in the evacuation chamber. When the chamber pressure drops below 10^{-6} Torr, 200Å of Al is evaporated onto the exposed surface. The evaporation is performed in an 18 inch N_2-cooled, diffusion-pumped system from a resistance heated W boat. Upon removal from the vacuum chamber, the specimen is glued to an Al disc (1/8 X 5/8 in. -- Fig.4.1) with conductive carbon paint (distributed by Ernst Fullam, Inc.). This disc which functions as backside contact, is fastened with a setscrew into the EBIC holder to assure a good ground contact. After the specimen has been examined in EBIC, it is easily detached from the disc by ultrasonic cleaning in acetone. If further treatment of the specimen (i.e., hydrogenation) is intended, the cleaning steps are repeated. The Al layer is removed completely by the HNO_3.

IV.C. PROCEDURE

A square array of nine diodes, each measuring about 0.25 cm on a side, was deposited on a section of ribbon material approximately 1 cm square. Diodes containing suitable defect structures were chosen by examination of the EBIC images. The specimen was then broken so that fractures crossed the bands of those defects that were relatively continuous in two of the diodes (see Fig.4.3). Three sections were chosen for study and labeled 1, 2, and 3 as shown, with diodes 1a (on section 1), 2a, 2b (on section 2), 3a, and 3b (on section 3). Specimen 1 (first section) was used as a control, being neither annealed nor hydrogenated, but having Al Schottky diodes deposited and removed along with the other two specimens.
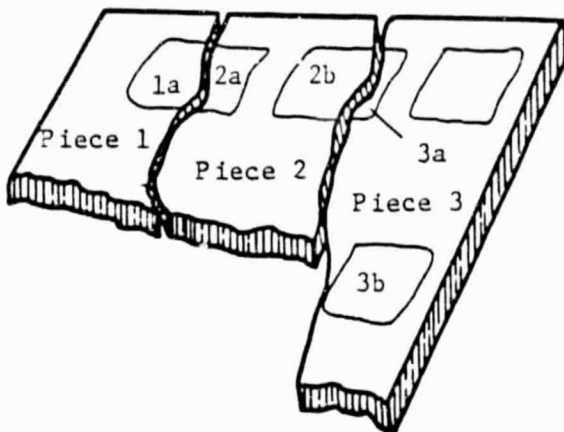
Fig. 4.3.

Illustration of the relationship between the breaks in the specimen and the diode position.

The second specimen (section 2) was annealed only once, and the third piece was hydrogenated to varying degrees. Table I shows the treatment schedule.

TABLE III. Specimen treatment schedule.

STEP	SPEC 1	SPEC 2	SPEC 3	DC RATIO: SPEC3/SPEC1
1	no treatment	200°C anneal 8×10^{-5} Torr 8 hr	200°C anneal 8×10^{-5} Torr 8 hr	1.4
2	"	no treatment	200°C anneal H plasma 2×10^{-3} Torr 8 hr 0.7 Torr 15 min	2.0
3	"	"	350°C anneal 1.5 Torr 16 hr	2.6-3.0
4	"	"	500°C anneal 8×10^{-5} Torr 12 hr	4

After each treatment, all three specimens were cleaned, HF etched and redeposited with new Al Schottky diodes. Designated regions were examined

under EBIC and quantitative parameters recorded. Then the Al was removed using the standard cleaning sequence and the specimens were subjected to the next treatment.

IV.D. RESULTS (LOW MAGNIFICATION)

STEP 1

FIG.4.4 is an EBIC micrograph comparing specimens 1 and 2 after specimen 2 was annealed in vacuum at $200^{o}C$. The EBIC current collected from specimen 2 is clearly greater than for the unannealed specimen 1; i.e., it is obviously brighter, and the profile of the collected current from a scan along the path located by the horizontal bright line in Fig.4.4 shows the image intensity to be about 40% greater on specimen 2. No significant differences were observed between specimens 2 and 3 (Fig.4.5) which were annealed simultaneously at $200^{o}C$.

STEP 2

After specimen 3 was hydrogenated at $200^{o}C$, the collected current increased by an additional 35% (Fig.4.6). Specimen 2 remained untreated after its initial $200^{o}C$ vacuum anneal, but had Schottky barriers removed and applied simultaneously with specimen 3.

STEP 3

Hydrogenation of specimen 3 at $350^{o}C$ for 16 hours at 1.5 Torr elevated the magnitude of the collected current by an additional 40% (Fig.4.7).

STEP 4

Finally, piece 3 was annealed for 12 hours at $500^{o}C$ in an 8×10^{-5} Torr vacuum in an attempt to evolve the hydrogen. Unexpectedly, a large increase, rather than a decrease, was observed in the collected current

Fig. 4.4. Specimens 1 (left) and 2 (right) after specimen 2 was annealed at 200°C. The superimposed charge collection profile was taken at the position shown by the bright line.
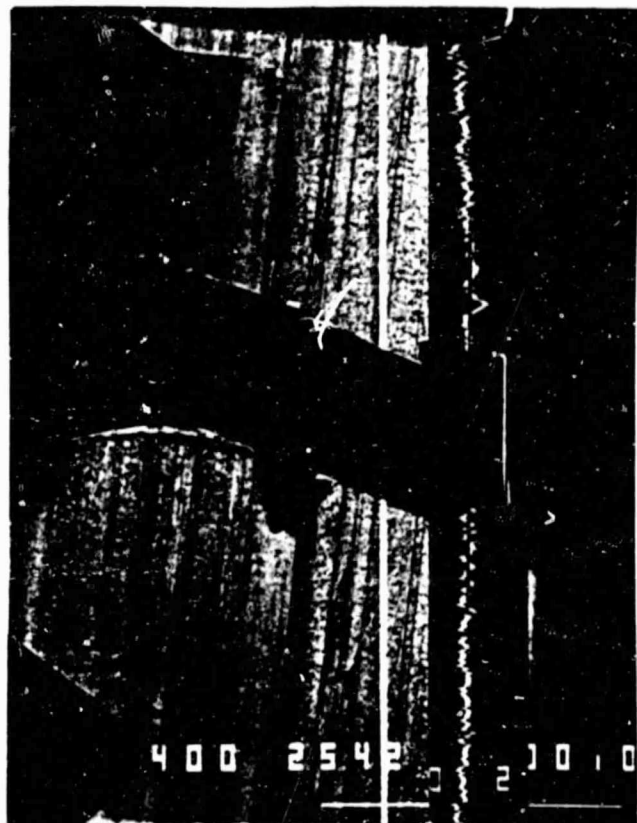
Fig. 4.5. Specimens 2 (left) and 3 (right) after both were annealed at 200°C in vacuum. Note that the charge collection profile shows no difference.

Fig. 4.6. Specimens 2 (left) and 3 (right) after specimen 3 was hydrogenated at 200°C. Charge collection profile shows increased collection from specimen 3.
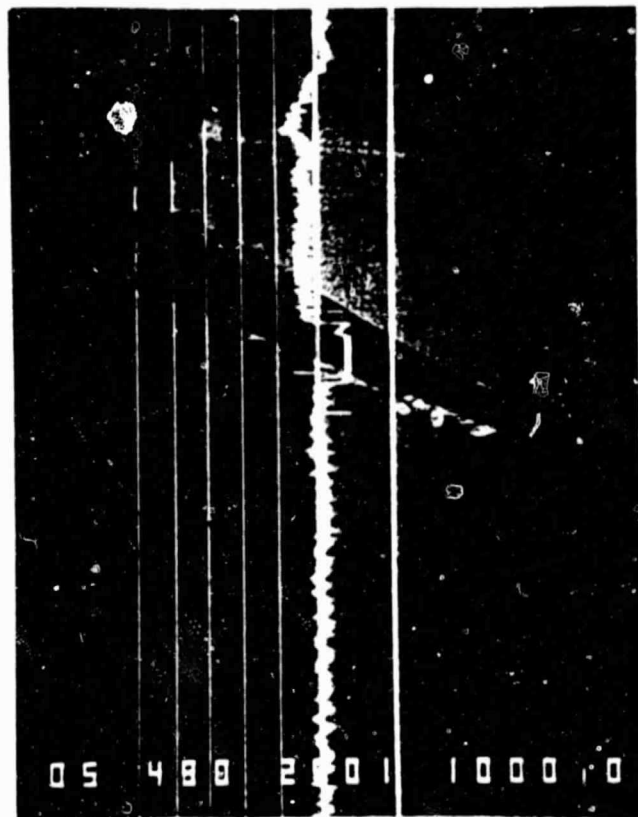
Fig. 4.7. Specimens 2 and 3 after specimen 3 (right) was hydrogenated at 350°C for 16 hr. Reference grid and charge collection profile are superimposed.

Fig. 4.9. Results of plasma and vacuum annealing on collected current (referred to collected current of nontreated specimen). Points are experimental values; dotted curve represents thermally induced changes in minority carrier lifetime (from [39]) normalized to fit the data.

Fig. 4.8. Specimens 2 and 3 after specimen 3 was annealed in vacuum (8 X 10^{-5} Torr) at 500°C for 12 hr.

(Fig.4.8). These results are summarized in Fig.4.9.

IV.E. ANALYSIS (LOW MAGNIFICATION)

The incident beam energy and beam current for the EBIC results presented thus far were E_b = 5KeV and I_b = 5 X 10^{-10} Amp, respectively. Hence from eqn. (2-5) and Fig.2.5, the electron range is R = 0.286 μm. The depletion 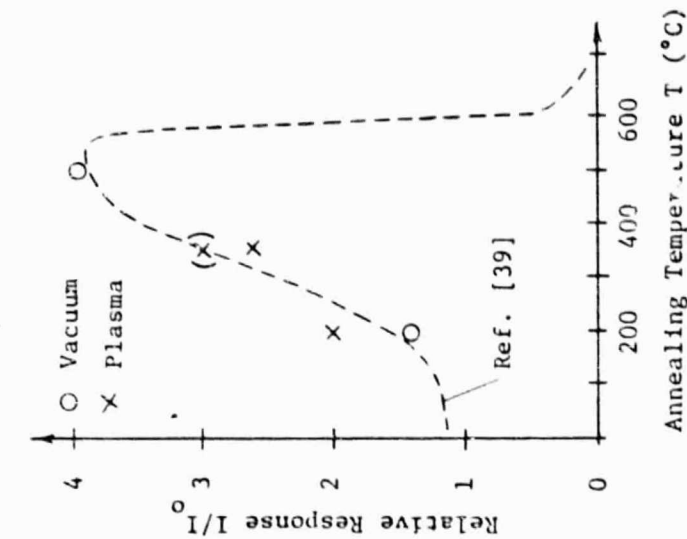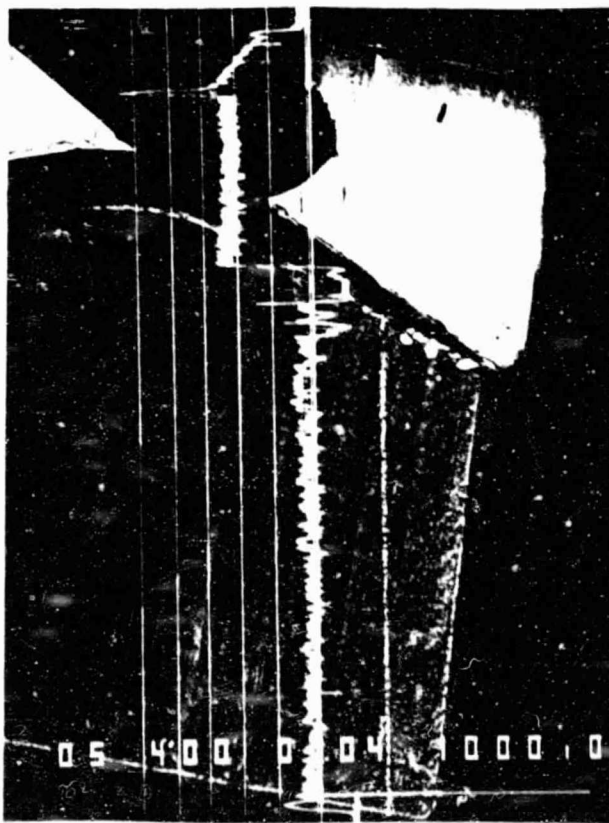layer width x_d = 2.68 μm [19] for 205 Ohm-cm material, i.e., the generation volume is contained completely within the depletion layer and is therefore under the influence of the built-in field. The situation is shown in Fig.4.10.
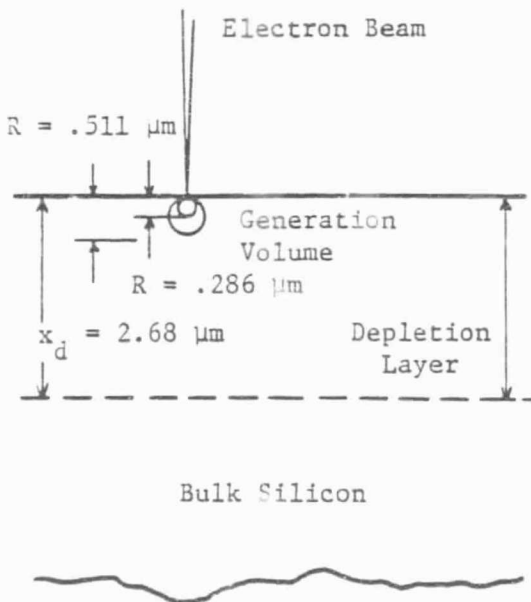

Fig. 4.10.

Relative dimensions -- generation volume diameter R and depletion layer width x_d, for 205 Ohm-cm Si and a beam energy E_B of 5 KeV.

The largest value for the collected current I_{cc} was observed in Fig.4.8. There the grid lines represent steps of one volt, i.e., the DC signal level is about 3 volts. Hence the magnitude of the collected

current is

$$(4\text{-}1) \qquad I_{cc} = V_{obs}/ \; X \; 10^8 \; (V/Amp)$$
$$= 3 \; X \; 10^{-8} \; Amp$$
$$= 60 \; I_b$$

where V_{obs} is the recorded DC signal level in volts and 10^8 (V/Amp) is the gain of the Keithley 427 fast current amplifier. The predicted value of collected current I'_{cc} from a corresponding perfect crystal is (eqn.(2-4))
$I'_{cc} = 1200 \; I_b$. Hence the maximum observed collection efficiency e_c is

$$(4\text{-}2) \qquad e_c = I_{cc}/I_{cc}' = (60/1200) = 0.05.$$

The lowest value of I_{cc} (observed in Fig.4.4) was only 25% as large, i.e., $e_c = 0.0125$. These are very low collection efficiencies compared to those predicted by Leamey et al [2] (see Fig.2.8). Part of this discrepancy can be explained by examination of the carrier lifetime within the depletion layer.

IV.1. CARRIER LIFETIME (DEPLETION LAYER)

First we shall assume that low-level injection conditions hold, and that the generation volume diameter is small compared to the separation between such localized defects as dislocations and grain boundaries, i.e., the collected current is characteristic of the bulk material. Under these conditions, the following expression [2] describes the collection efficiency e_c when the generation volume is entirely contained within the depletion layer.

$$(4\text{-}3) \qquad e_c = [1-\exp(- \gamma)]/\gamma, \qquad \gamma = R/(v_d \tau).$$

Here v_d is the drift velocity in the built-in field, and τ is the minority

carrier lifetime. Fig.4.11 shows e_c as a function of τ for two values of

R = .236 μm

R = .571 μm

$$\eta = \frac{1 - e^{-\gamma}}{\gamma}$$

$$\gamma = \frac{R}{v_d \tau}$$

τ = 1.6 psec

e_c(0.16 psec) = 0.5

e_c(0.16 psec) = 0.13

Carrier Lifetime τ (psec)

Charge Collection Efficiency e_c
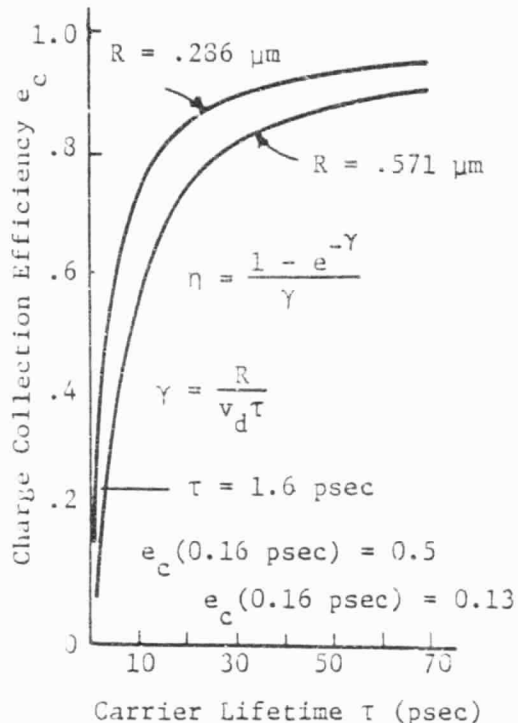
Fig. 4.11.

Collection efficiency as a
function of carrier lifetime
for $R < x_d$.

the electron range: R_1 = 0.286 μm and R_2 = 0.572 μm (these two values are

the most often favored in the range calculations). Using the larger value

of R, the efficiencies of 0.05 and 0.0125 correspond to lifetimes of 0.64

psec and 0.16 psec, respectively. These values are unreasonably small,

even when compared to lifetimes of 1-10 nsec found in poor quality

polysilicon ribbon.

A calculation of the injected carrier density is straightforward. For

a spherical generation volume

$$(4-4) \quad e/V = (I_{inj}\tau)/qV$$
$$= (1200 \, I_b \tau)/[(4/3) \, \pi \, r^3 \, q]$$
$$= (1200)(5 \times 10^{-10} \, A)(10^{-9} \, s)/(4.2)(R/2)^3(1.6 \times 10^{-19} \, C)$$

$$= 3.07 \times 10^{17} \ e^-/cm^3, \quad r_1 = R_1/2 = 0.143 \ \mu m$$
$$= 3.83 \times 10^{16} \ e^-/cm^3, \quad r_2 = R_2/2 = 0.286 \ \mu m$$

where a bulk lifetime of 1 nsec was used and the calculation is done for both values of the range. Since the bulk doping level is about $10^{14}/cc$, we are clearly operating in the high-level injection regime. Furthermore, the actual carrier densities could be two orders of magnitude greater, depending on the actual value of the bulk lifetime. Hence according to Fig.2.7, the effective lifetime is between 1 and 10 psec.

Miller et al [24] suggested that an additional effect occurs for high carrier densities within the depletion layer -- the carriers in the generation volume form a highly conductive plasma which retains its integrity for nearly 10 nsec. Carriers at the plasma boundary polarize slightly, excluding the built-in field from the plasma interior. Carriers are gradually lost through erosion at the plasma surface, but during the existence of the plasma, carriers in its interior interact as they would in bulk Si beyond the depletion layer. In this case a bulk lifetime of 100 nsec would correspond to an effective lifetime of 0.1 nsec or less within the plasma, such that a two order magnitude reduction in carrier population prior to the collapse of the plasma is not improbable. Extended analysis of this effect is beyond the scope of this paper. However, this qualitative discussion shows that the observed collection efficiencies are not unreasonable for the beam conditions and specimen used.

As discussed in Ch.II.D.1., the reduction in lifetime at high carrier concentrations is due to traps near the band edges, typically the doping levels and a restricted class of defects. The reduction in lifetime is more pronounced at lower trap concentrations at a given excess carrier

concentration. Hence removal of a substantial fraction of these traps by hydrogenation would be expected to reduce the effective lifetime rather than to increase it, and would lead to reduced current collection. Since the opposite was observed, hydrogenation probably does not affect these states. However the effective lifetime can be increased by increasing the bulk lifetime, and the bulk lifetime can be increased by decreasing the concentration or cross section of recombination centers since

$$(4-5) \qquad \tau_o = 1/(\sigma v_{th} N_t)$$

where $\sigma (cm^2)$ is the cross-section of the recombination center, v_{th} (cm/sec) is the electron thermal velocity, and N_t is the concentration of recombination centers. Very little is known about the influence of hydrogen on the cross-section, but in principle it is possible that hydrogen could decrease both σ and N_t. Since the results of Pankove et al [31] (see Ch.III) indicate that hydrogenation affects the defect states clustered near midgap, a bulk lifetime increase through this mechanism seems plausible. Hence a mechanism exists whereby hydrogenation can cause an improvement in the bulk collection efficiency.

IV.2. THERMAL EFFECTS

The 40% increase in I_{cc} from specimen 2 after vacuum annealing at $200^{\circ}C$ shows that another phenomenon is competing with the hydrogenation in extending the lifetime. Since controls for thermally induced changes were not included in the hydrogenation work reviewed in Ch.III, no changes had been expected when specimen 2 was merely annealed. The 40% increase in response that was observed was a surprise. A proper study of thermal influences was not carried out then, however, because no additional control

specimens were available. Graff et al [39] have reported lifetime increases by up to a factor of five over the temperature range 0-600°C, for 10 Ohm-cm float-zone p-type single crystal Si. They postulate that oxygen complexes bind to impurities associated with traps, deactivating the traps. More traps are removed as temperature is increased up to 600°C. Temperature elevations beyond 600°C break the bonds to the impurities in order for the complexes to form a different structure, and the impurities are precipitated back out as recombination centers. Fig.4.12 shows the
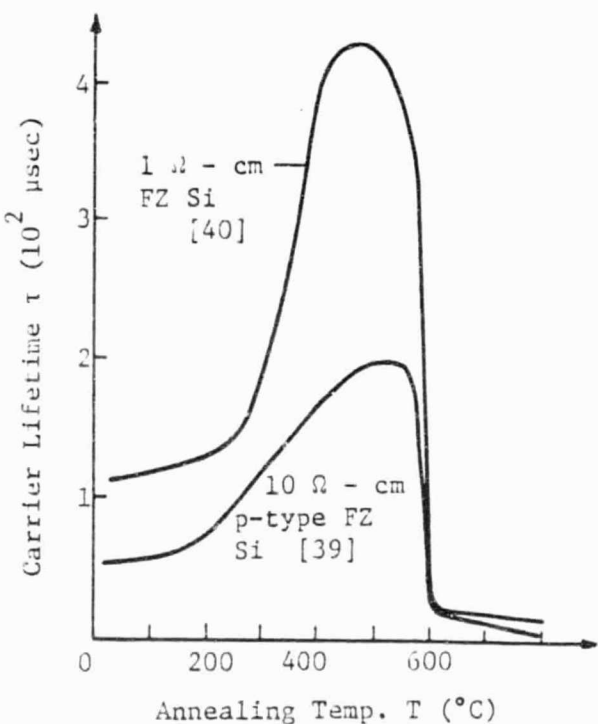
Fig. 4.12.

Minority carrier lifetime τ as a function of annealing temperature for $1\ \Omega - cm$ [40] and $10\ \Omega - cm$ [39] Float-zoned Si.

results of Graff et al along with results for 1 Ohm-cm float-zone Si reported by Fischer et al [40]. Graff et al cite work of other investigators that found smaller increases in lifetime in material with a dislocation density of 10^4/cc. Our material differs from Graff's in many ways, particularly in that it has a high Carbon (C) content and a higher dislocation density. It is conceivable that the lifetime increases

reported above represent an upper limit to what we should expect, and our actual increase might be reasonably expected to be substantially less than fourfold.

Hydrogenation at 200°C of specimen 3 after the 200°C vacuum anneal with specimen 2 produced an additional increase in collected current. This increase could have resulted from the additional 8 hours of annealing, but in view of previously described hydrogenation effects, this increase is more probably due to the hydrogenation.

Several possibilities exist to explain the observation that the final vacuum anneal produced a large increase in collected current. Since Pankove et al [31] and Lam [32] report H evolution at 550°C, another possible explanation for the absence of a decrease in I_{cc} is that the 500°C was insufficient to evolve a substantial amount of H. However, this explanation appears less likely, because higher magnification images (to be discussed in greater detail below) of the same region before and after the final anneal show large decreases in I_{cc} at selected defects after the anneal, indicating that substantial evolution occurred.

The results of Graff et al [39] (normalized to τ (25°C)), superimposed on the data in Fig.4.9, correspond remarkably well including at 500°C where a reduction was expected. This correspondence may indicate that effects due to hydrogenation are simply added to the thermally induced changes. No firm conclusions on these points can be made without a better separation between the thermal and chemical contributions, because of the differences between EFG and float-zoned material.

However, it can be concluded that (i) thermal effects are important and (ii) they must be separated out from hydrogenation if the latter is to be studied properly.

V. OBSERVATIONS AT HIGH MAGNIFICATION

V.A. STRESS INDUCED DISLOCATIONS

A family of structures having characteristics of stress-induced dislocations first appeared on diode 3b (specimen 3 -- see Fig.4.3) after the vacuum anneal at 200°C. As indicated by the arrows in Fig.5.1a, they are suggestive of a scratch. Their appearance became less uniform and intense after the hydrogenation at 200°C (Fig.5.1b), and after the 350°C hydrogenation, more interesting details became visible (Fig.5.1c). Fig.5.2 shows the portion of the scratch indicated in Fig.5.1c, magnified to 1000X. The scratch itself is narrow and is visible at the left of the micrograph (just below the white horizontal line which marks the linescan position) as a line normal to the central portions of the dislocations. The heavy vertical lines (horizontal in Fig.5.1) extending from top to bottom are second order 111/115 twins or first order coherent microtwin boundaries.

We know that the ribbon surface is most probably (110) [41] and that coherent twin boundaries in EFG always have {112} traces, i.e., {112} is the direction along which each of the two <111> planes perpendicular to the (110) plane intersect the surface. Fig.5.3a shows all of the angles produced by projection onto the (110) plane of the possible dislocations in (111) planes in Si. Two possible configurations (Figs.5.3b and 5.3c) have angles in the ranges found in Fig.5.2. Configuration 5.3b probably does not apply to this case because any dislocation along the [110] direction would remain parallel to the surface, while the segments at each end of the dislocation must terminate at the surface (Fig.5.4). If configuration 5.3c is correct, the depth of the main segment of the dislocation can be estimated geometrically. The right and central segments of the dislocation
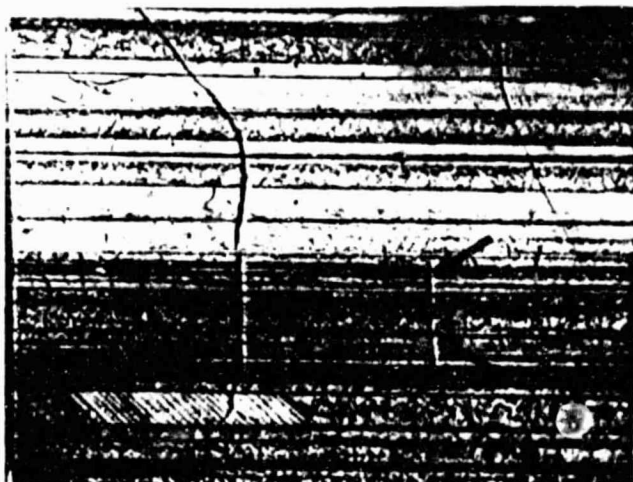
71

Fig. 5.1a.

Diode 3b with scratch. EBIC micrograph (44X) after 200°C vacuum anneal.

Fig. 5.1b.

EBIC micrograph of same area as shown in part a) after hydrogenation at 200°C.

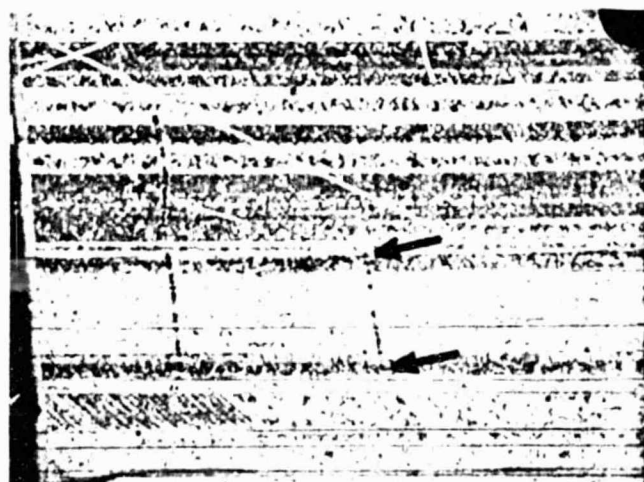Fig. 5.1c.

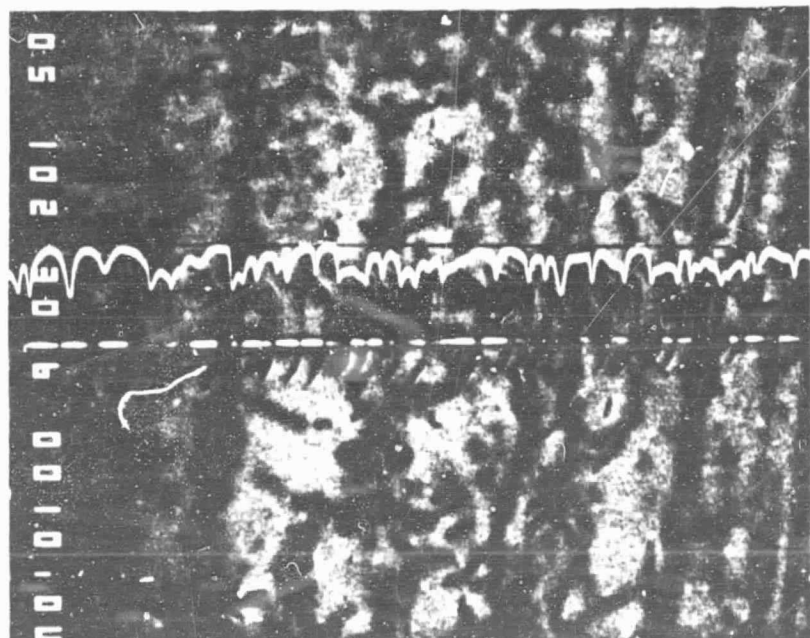EBIC micrograph (200X), after hydrogenation at 350°C. Arrows in a) and b) indicate the area shown in c).

Fig. 5.2. 1000X EBIC micrograph of the portion of
the scratch indicated in Fig. 5.1c.
The actual scratch line runs horizon-
tally across the picture just below
the bright line.
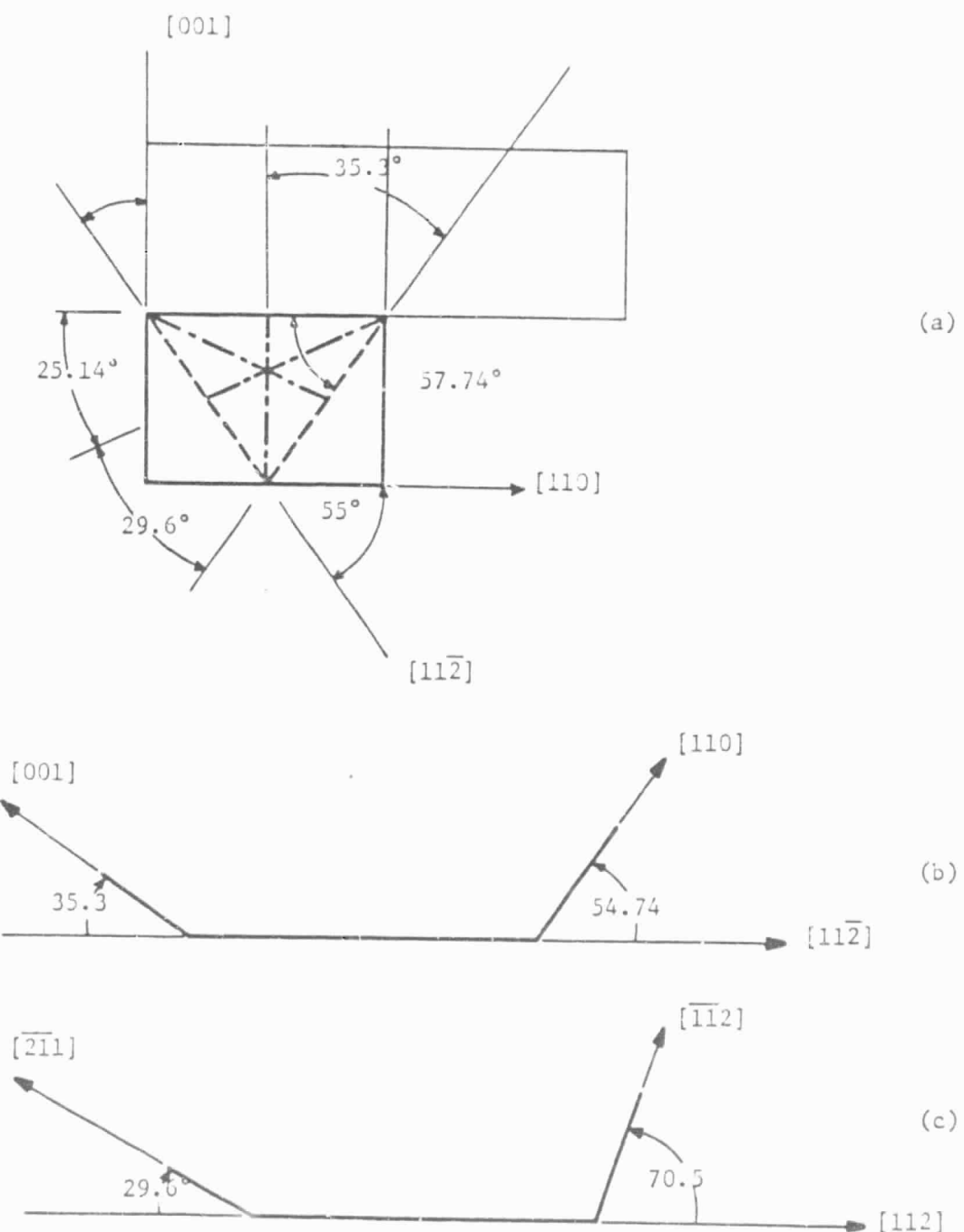
Fig. 5.3. Possible geometric configurations for projection of
a dislocation image onto a (110) surface.

$[\overline{11}2]$

$[11\overline{2}]$

70°

(110)

$[\overline{2}\overline{1}1]$

$d = b \tan 30°$
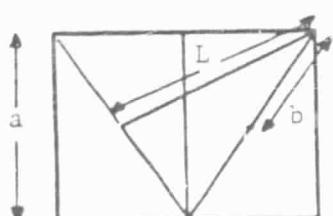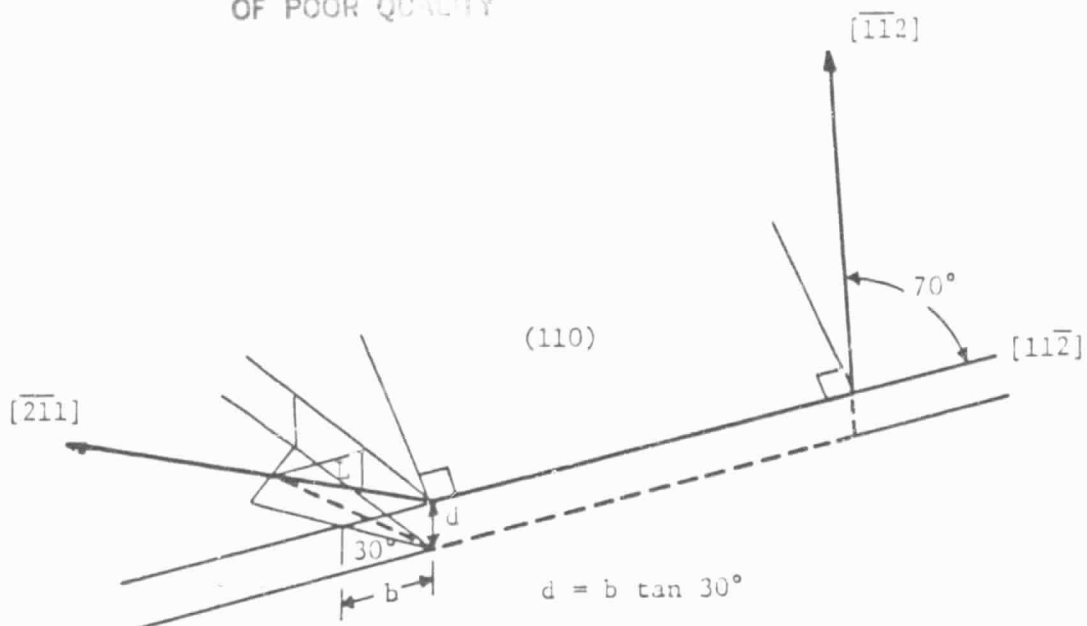
$$L = \left[\frac{a^2}{4} + \frac{9a^2}{8}\right]^{\frac{1}{2}} = \frac{a}{2}\left(\frac{11}{2}\right)^{\frac{1}{2}}$$

$$b = \left[\frac{1}{2} a^2 + \frac{a^2}{2}\right]^{\frac{1}{2}} = \frac{a}{2}\left(\frac{3}{2}\right)^{\frac{1}{2}}$$

$$b = 0.52 \; L \qquad L \simeq 2 \; \mu m$$

$$d = .52 \; L \; (.58)$$

$$= 0.3 \; L$$

$$= 0.6 \; \mu m$$

Fig. 5.4. Possible slip systems for stress-induced disloca-
tions, and the geometry used for estimation of
the depth of the central segment.

move in a direction normal to the surface on the two <111> planes which are perpendicular to the surface, i.e. their projections onto the (110) surface reveal nothing about their depth. The left segment, however, moves on a <111> plane inclined 30 degrees with respect to the surface as illustrated in Fig.5.4. Hence we can calculate the depth of the left end of the central segment from the measured length of the left segment. Using the geometry in Fig.5.4, the depth d is expressed as

$$(5-1) \qquad d = L \ (.52)(\tan 30^{\circ})$$
$$= 0.3 \ L$$
$$= 0.6 \ \mu m.$$

If the built-in field actually confines all excess carriers to the generation volume as discussed in Ch.II, the electron range $R = 0.286 \ \mu m$ predicted by Everhart and Hoff [14] is not sufficient to image these defects, while $2R = 0.572 \ \mu m$ a value favored by Mareck [28], is close. However, given the likelihood that within the depletion layer a plasma exists which acts to exclude the built-in field from its interior, some degree of electron diffusion beyond R seems probable. Support for this conjecture will be presented in the following discussion.

V.B. DEPTH PROFILING BY BEAM VOLTAGE VARIATION

For the case $R > x_d$, Donolato [26] showed that for a point defect at a depth d, both the contrast and image width vary strongly with R/d. Contrast peaks and image width is at its minimum for R/d = 1.2. For R/d > 1.2, contrast decreases rapidly with increasing range R, and image width increases. Since Donolato subsequently showed that a dislocation can be treated successfully as a linear array of point defects, dislocation images

might be expected to abide qualitatively by these rules. Hence for a dislocation parallel to the surface, an optimum in image width and contrast should occur for R = 1.2 d. Contrast should be lighter for d > R and image width should grow linearly with d for constant beam energy. Inclined dislocations thus would be expected to have intense images of narrow width nearest the surface, and broader and more diffuse images with increasing depth, as reported in reference [2]. If the beam energy is increased, the generation volume will penetrate deeper, sharpening more of the image near the surface and extending the length of the diffuse contrast. But since increasing the beam energy also increases the generation volume diameter, the image width of the sharp portion will also have increased.

For low-level injection and R << x_d, all excess carriers outside of the generation volume are presumably swept away by the built-in field. Hence the image width is strictly defined by the generation volume diameter, and the image of an inclined dislocation should terminate rather abruptly beyond R. If, for the high-level injection regime, exclusion of the built-in field by the plasma of carrier pairs allows carrier diffusion beyond R, images may behave in a way that is qualitatively similar to that predicted by Donolato's theory for R > x_d.

In order to test this hypothesis, the portion of the scratch immediately to the right of that shown in Fig.5.2 was selected for examining changes in contrast and image width as a function of R. Figs.5.5a&b, 5.6a&b, and 5.7a&b are micrographs of this region taken at beam energies of Eb = 5, 7, 10, 15, 20, and 30 KeV, respectively. Magnification (1000X) and beam current (I_b = 5 X 10^{-10} Amp) were held constant for all six micrographs. Generation volume diameters and electron ranges (calculated according to Everhart and Hoff [14]) are given below

78

Fig. 5.5a. E_B = 5 KeV

R = 0.286 µm
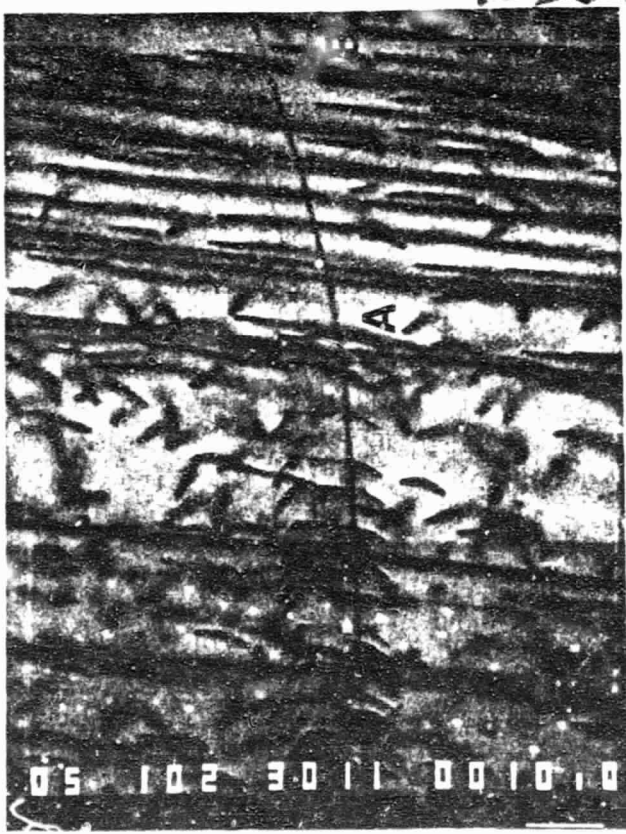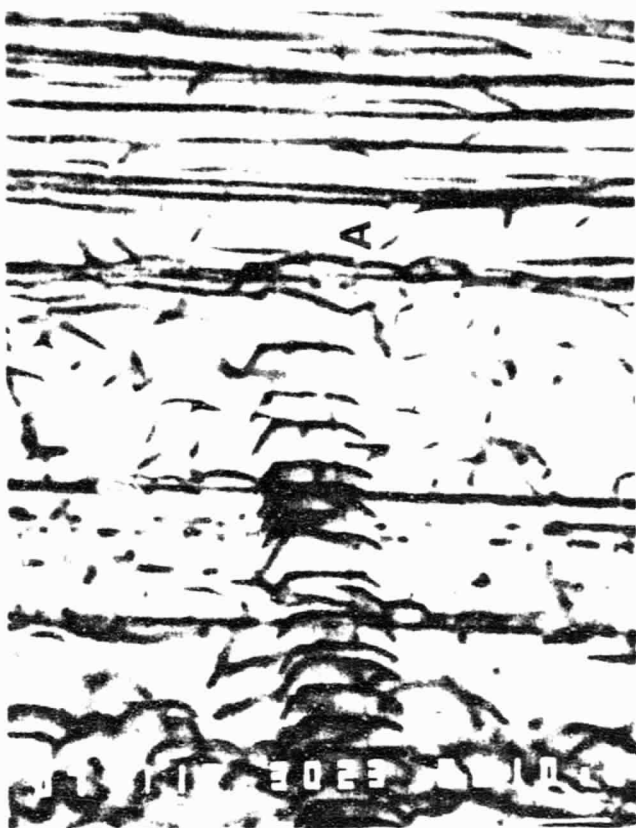
— Generation volume diameter

Fig. 5.5b. E_b = 7 KeV

R = 0.52 µm

Generation volume diameter ⟶

Fig. 5.6a. E_b = 10 KeV
R = 0.96 μm
Generation volume diameter
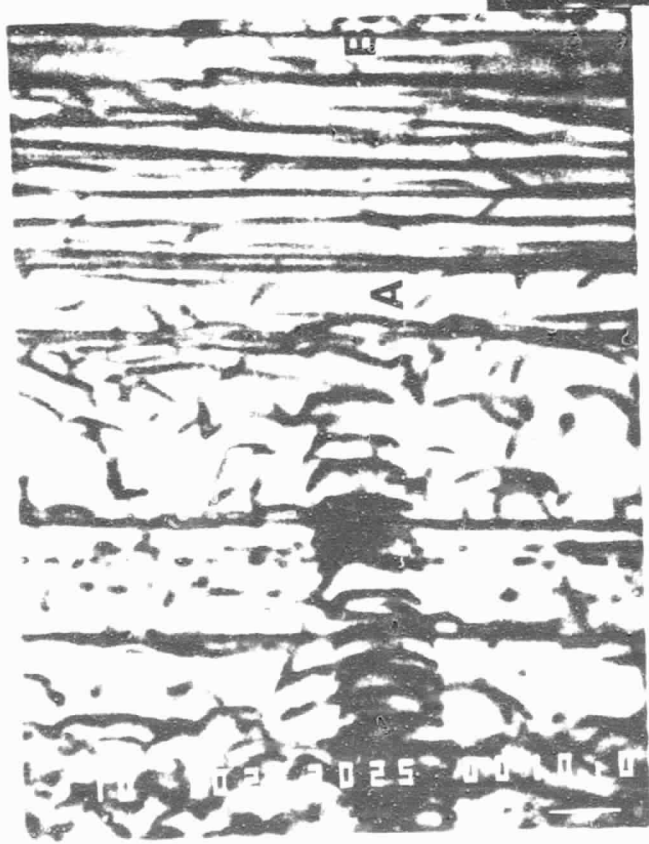
Fig. 5.6b. E_b = 15 KeV
R = 1.97 μm
Generation volume diameter ——→ O

Fig. 5.7a. E_b = 20 KeV

R = 3.23 μm

○ ——→ Generation volume diameter

Fig. 5.7b. E_b = 30 KeV

R = 6.58 μm

◯ ——→ Generation volume diameter

each micrograph.

The first observation from these six micrographs is that the image widths of the stress-induced dislocations are about equal to the diameter of the generation volume in all cases, in agreement with both Donolato's theory and the range formula of Everhart and Hoff. But the theory is based upon the uniform sphere approximation to the generation volume, which would imply that the electrons penetrate to only about 0.3 μm. This was shown above to be inadequate to image the stress-induced dislocations. Hence the generation volume cannot be spherical, and would appear to have a depth at least twice its diameter.

The second observation is that the images of the surrounding grown-in defects broaden in a nonuniform way. The defect to the right of the letter B (right side of all micrographs but 5.6a) remains at a nearly constant width until E_b = 15 KeV where it begins to broaden. As the image broadens, the contrast near the edges of the image becomes diffuse while that at the center of the image remains dark. At E_b = 30 KeV only the dark contrast is visible and the image width actually appears smaller than it was at 5 KeV (Fig.5.5). A similar pattern is followed by several of the long vertical defects (probably dislocations) just to the right of the letter A. An explanation may be provided by Fig.2.6b [17] which shows the generation volume as teardrop in shape, with a narrow neck near the surface. Energy dissipation profiles indicate that carrier pair creation density is greatest in the long narrow region whose diameter roughly corresponds to the neck diameter. Thus in Fig.5.7b where $R > 2x_d$, the effective generation volume diameter within the depletion layer could be much smaller than R. The minimum image width theoretically attainable under these conditions would be equal to the spot size of the incident beam on the

specimen, which is about 100A for the JEOL 733. It is therefore possible for the same defect to produce a narrower image at 30 KeV than at 5 KeV.

An extreme example of this is shown in Fig.5.8, taken from a different region of the same diode at a beam energy of 20 KeV and a magnification of 5400X. A fine line of lighter contrast is seen to run diagonally across the left side of the micrograph, from upper left to lower right (see arrows). This line, as seen in other photographs, travels in a <112> direction and is quite straight. These facts together indicate that this is probably a microtwin boundary perpendicular to the surface. The enhanced contrast of this line relative to its immediate surroundings could be due to defect-free crystal between twins and defects outside the twins. Note that the width of the dark contrast within which the lighter line lies is about as large as the generation volume diameter (as usual). The remarkable feature is that the width of the line is about 0.1 μm (1000Å) while the generation volume is more than thirty times (3.23 μm) greater. A possibility also exists that this contrast is topologically produced by enhanced secondary emission or backscattering at surface features, but no evidence of this was observed when Fig.5.8 was made.

Since $R > 2x_d$ in Fig.5.7b, most of the generation volume extends beyond the bottom of the depletion layer. The image width of defects within the depletion layer is then determined by the diameter of the portion of the neck that encounters the defect. In Fig.5.6b, however, at least half, and maybe all, of the generation volume is still contained within the depletion layer. The neck therefore will not be a factor in the image width, but the nonuniform distribution of the carrier pairs will. This effect is not usually observed because standard imaging conditions use beam currents 10-100 times larger, $E_b > 10$ KeV, and materials with

Fig. 5.8. Microtwin boundary along [112] direction and perpendicular to the specimen surface. EBIC; 5400X.
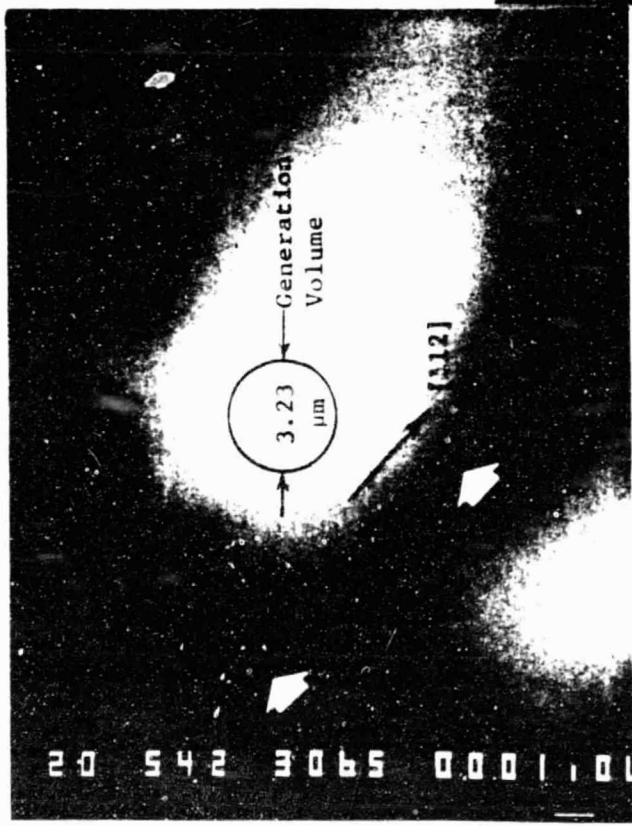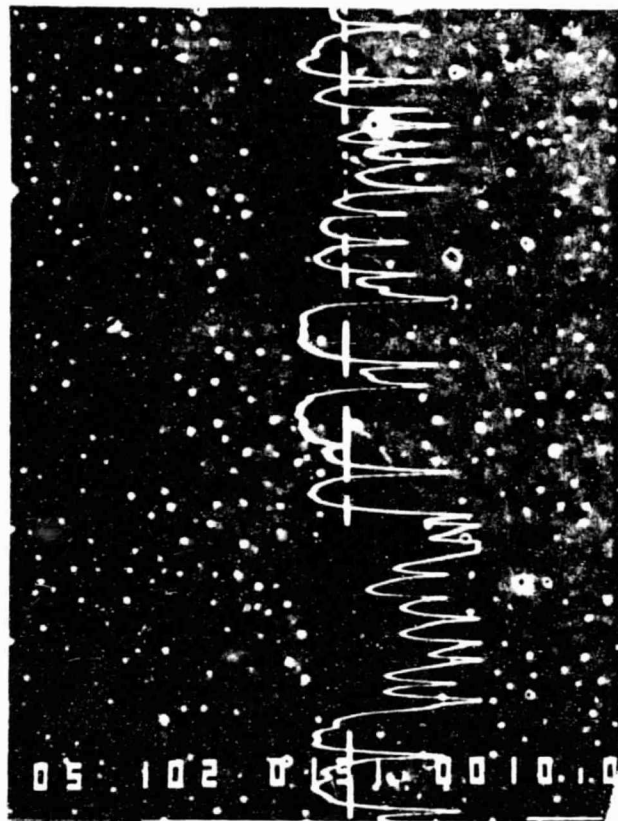

Fig. 5.9. Same area as shown in Fig. 5.2, after annealing for 12 hr. in vacuum at 500°C. Note especially the relative change in contrast between the stress-induced dislocations and those in the background.

resistivities between 1 and 10 Ohm-cm; i.e. $R > x_d$ and Donolato's theory applies. The beam current used in our work was the smallest that could be reliably detected by the Faraday cage. The large depletion layer and constant beam current allowed observation of image behavior for changes in carrier density over four orders of magnitude.

The third important observation to be drawn from these micrographs is that inclined defects in the depletion layer can produce the same kind of images they would produce beyond it, as illustrated by the dislocation just below the letter A. The width of this image decreases as R increases until $R = 0.96$ μm (Fig.5.6a). Similar behavior is shown by several other defects, including the vertical dislocation immediately above the letter A. If the range R were correct, these dislocations would be about 1 μm deep. The defect below A does not lengthen with increasing R, but grows a curved tail which is very visible in Fig.5.6b, indicating that the dislocation probably continues deeper into the crystal. The existence of the diffuse tails on the inclined dislocations, and the sharpening of contrast with increasing R for the dislocations parallel to the surface, indicate electron penetration of two to four times that predicted by R. It is interesting to note here that the results of Everhart and Hoff [14] began to diverge at about 8 KeV (for unknown reasons), suggesting that their expression for R may not apply for these low energies.

V.C. EFFECTS OF HYDROGENATION

The stress-induced dislocations provided a very useful tool to evaluate the effects of hydrogenation and dehydrogenation. Fig.5.2 shows these dislocations after hydrogenation at 350°C. Fig.5.9 shows the same

region after being annealed in vacuum at 500°C. Comparison of the linescans between the two figures shows greatly increased contrast in the latter figure, indicating a large increase in recombination. Current collection is seen to drop occasionally to zero. The contrast of the grown-in defects surrounding the stress-induced defects has changed little in comparison, as can be observed wherever the linescan crosses one. Fig.5.10 shows linescans across a row of dislocations on another area of the same diode both before and after the 500°C vacuum anneal. The contrast changed only slightly in comparison to that of the stress-induced dislocations. If hydrogenation is assumed to have evolved from broken bonds in the stress-induced dislocations, the comparative absence of change in the contrast of the grown-in dislocations suggests an absence of dangling bonds. These dislocations therefore may be reconstructed and/or may have impurity atoms other than H already occupying the broken bonds. The stress-induced dislocations, on the other hand, would necessarily form broken bonds during the glide process. Furthermore, high stress deformation at low temperatures has been shown to generate dissociated dislocations [42], [43], and electrical recombination efficiency of edge dislocations has been observed to be enhanced under dissociation [44].

Another variable not considered so far, is the depth of the grown-in dislocations. Other micrographs (not shown here) of dislocations parallel to the surface (also on this same diode) appear to display increased recombination after the 500°C vacuum anneal. Their depth is unknown because no quantitative tests were performed. Thus, since all of the grown-in dislocations examined with a linescan were sharply inclined relative to the surface, it is possible that hydrogen only evolved from the near-surface region and that further annealing at 550°-600°C would produce

Fig. 5.10a. Charge collection profiles (EBIC, 1000X) across a row of "dislocations" after hydro-generation at 350°C.
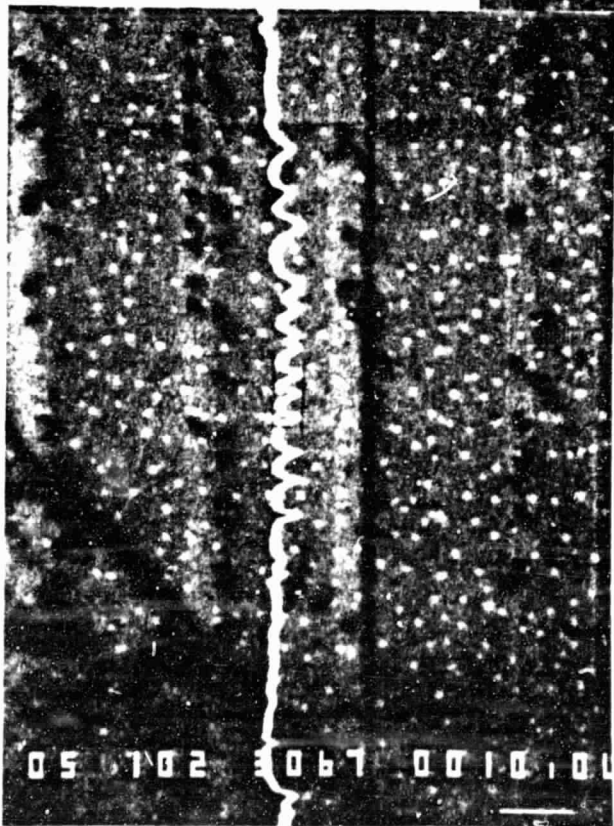

Fig. 5.10b. Charge collection profiles across the same dislocations after annealing at 500°C in vacuum. No differences are evident that might be attributed to hydrogen evolution.

more spectacular results. These results are ambiguous because of the unknown extent of the thermal increase in lifetime.

VI. SUMMARY

Quantitative EBIC has been used to measure the effects of hydrogenation on polysilicon ribbon. Low beam energy and small beam currents were used to obtain acceptable resolution at high magnification (5400X) in order to examine the effects of hydrogenation on the defect structure of the ribbon in greater detail than has been done previously.

Hydrogenation was shown to passivate stress-induced dislocations to a high degree. Its effect on grown-in defects remains ambiguous because of superimposed thermal effects. Bulk minority carrier lifetime appears to have been increased by a factor of four by the hydrogenation treatment, but much of this increase can be attributed to thermal effects. The contrast of the passivated dislocations did not entirely disappear possibly due to decoration by residual impurities.

The uniform sphere approximation for the generation volume was found not to be accurate inside the depletion layer for a beam energy of 5 KeV and a beam current of 5×10^{-10} Amp. Careful analysis of micrographs magnified 1000X indicated that the effective length of the generation volume was at least twice its diameter, and that carrier pairs were generated most densely around the beam axis. The generation volume appears to neck down near the surface, in agreement with the teardrop shape hypothesized by Herzog et al [17]. In addition, carriers appear to diffuse in significant quantities beyond the borders of the generation volume, even when the generation volume is completely contained in the depletion layer.

In future work, the thermal and chemical influences on lifetime must be separated before the effects of hydrogenation on a complex material like EFG can be properly assessed. High resolution EBIC will also require a more accurate understanding of the structure of the generation volume in the depletion layer.

BIBLIOGRAPHY

1. S. M. Davidson, J. of Microscopy, Vol. 110, Pt. 3, 177-204 (Aug. 1977).

2. H.J. Leamey, L.C. Kimmerling, S.D. Ferris, SCANNING ELECTRON MICROSCOPY/1976 (Part IV) -- Proc. of the Workshop on Micro-electronic Device Fabrication and Quality Control with SEM, Chicago, 1976, pp. 529-538.

3. J. Heydenreich, H. Blumtritt, R. Gleichmann, H. Johansen, Journal de Physique, colloque C6, Supplement au n6, tome 40, juin 1979, C6-23 to C6-26.

4. H. Strunk, B. Cunningham, D. Ast, in "Defects in Semiconductors"; MAS Symposia Proc. Vol. 2, Boston, 1980. Ed. J. Narayan, T. Y. Tan, North-Holland, pp. 297-302.

5. E. J. Sternglass, Phys. Rev., Vol. 95, No. 2, 345-358 (15 Jul. 1954).

6. H. E. Bishop, Britt. J. Appl. Phys., Vol. 18, 703-715 (1967).

7. F. K. Richtmeyer, E. H. Kennard, J. N. Cooper, "Introduction to Modern Physics", 6th ed., McGraw-Hill, 1969, pp.420-421.

8. Ibid. p. 412.

9. I. Lindau, W. E. Spicer, J. Electron Micros. & Related Phenomena. Vol. 3, 409-413 (1974).

10. W. Czaja, J. Appl. Phys., Vol. 37, No. 11, 4236-4248 (1966).

11. W. Shockley, Czech. J. Phys., Vol. B11, 81-121 (1961).

12. G. Fabri, E. Gatti, V. Svelto, Phys. Rev., Vol. 131, No. 1, 134-136 (Jul. 1963).

13. See for example S. M. Davidson, J. of Microscopy, Vol. 110, Pt. 3, 117-204 (Aug. 1977).

14. T. E. Everhart, P. H. Hoff, J. Appl. Phys., Vol. 42, No. 13, 5837-5846 (Dec. 1971).

15. A.E. Gruen, Z. Naturforch., 12A, p.89 (1957).

16. R. Shimizu, T. E. Everhart, Optik, Vol. 36, 59-65 (1972).

17. R. F. Herzog, J. S. Greeneich, T. E. Everhart, T. Van Duzer, Record of the 11th Symposium on Electron , Ion and Laser Beam Technology (R. F. M. Thornley ed.); San Francisco Press, Inc., 483-494 (1971).

18. T. E. Everhart, R. F. Herzog, M. S. Chung, W. J. DeVore, Proc. 6th International Conf. on X-ray Optics and Microanaylsis, pp. 81-86.

19. A. S. Grove, "Physics and Technology of Semiconductor Devices", Wiley, NY (1967), P. 159.

20. Ibid., p. 159.

21. Ibid., P. 108.

22. W. Snockley, W.T. Read, Jr., Phys. Rev.,87 (5), 835-842 (1 Sept. 1952).

23. G.L. Miller, W.M. Gibson in: "Nuclear Electronics I", Int. Atomic Energy Agency, Vienna,1962, pp.477-493.

24. G.L. Miller, W.L. Brown, P.F. Donovan, I.M. MacKintosh, IRE Trans. Nucl. Sci. NS-7 (2-3), 185-189 (1960).

25. H. J. Leamy, L. C. Kimmerling, S. D. Ferris, Scanning Electron Microscopy 1978/ Vol. I, SEM Ind., AMF O'Hare, IL, 60666, 717-726.

26. C. Donolato, Optik, Vol. 52, No. 1, 19-36 (1978/79).

27. C. Donolato, Appl. Phys. Lett., Vol. 34, No. 1, 80-81 (Jan. 1979).

28. J. Marek, J. Appl. Phys. 53 (3), 1454 (Mar. 1982).

29. C.H. Seager, D.S. Ginley, Appl. Phys. Lett., 34 (5), 337-340 (1 Mar 1979).

30. J.L. Benton, C.J. Doherty, S.D. Ferris, D.L.Flamm, L.C. Kimmerling, H.J. Leamey, Appl. Phys. Lett., 36 (8), 670-671 (15 Apr 1980).

31. J.I. Pankove, M.A. Lampert, M.L. Tarng, Appl. Phys. Lett., 32 (7), 439-441 (1 Apr 1979).

32. H.W. Lam, Appl. Phys. Lett., 40 (1), 54-55 (Jan 1982).

33. See for example, "Foundations of Plasma Dynamics", by E. H. Holt, R. E. Haskell, MacMillan, NY, 1965; or "Plasma Diagnostics with Microwaves" by M. A. Heald & C. B. Wharton, Robert Krieger, NY, 1978.

34. D. A. Frank-Kamenetskii, "Plasma the Fourth State of Matter", Plenum Press, NY, 1972, p. 12.

35. T. Makino, H. Nakamura, Appl. Phys. Lett., Vol. 35, (7), 551-552 (1979).

36. J.Y.W. Seto, J. Appl. Phys., 46 (12), 5247-5254 (1975).

37. D. G. Ast, T. Sullivan, "Preparation of Schottky Diodes for EB. Investigation of Grain Boundary Passivation in Si Ribbons", J.P.L. Report No. 3, (1979).

38. C.H. Seager, D.S. Ginley, J.D. Zook, Appl. Phys. Lett., 36 (10), 831-833 (1980).

39. K. Graff, H. Peiper, G. Goldbach, "Semiconductor Silicon 1973", 170-178.

40. H. Fischer, W. Pschunder

41. L. C. Garone, C. V. Hari Rao, A. D. Morrison, T. Surek, K. V. Ravi, Appl. Phys. Lett., 29, (8), 511-513 (1979).

42. H. Alexander, Journal De Physique. Colloque C6, supplement au n° 6, tome 40, juin 1979. C6-1.

43. K. Wessel, H. Alexander, Phil. Mag. 35 (6), 1523-1536 (1977).

44. A. Ourmazd, G. R. Booker, Phys. Stat. Sol. (a) 55, 771 (1979).

C-2